Surface electronic structure: Embedded self-consistent calculations

J. E. Inglesfield
Daresbury Laboratory, United Kingdom Science and Engineering Research Council Daresbury, Warrington WA4 4AD, England

G. A. Benesh
Department of Physics, Baylor University, Waco, Texas 76798
(Received 8 September 1987)

A new, self-consistent, full-potential method of determining surface electronic structure is described in which the surface atomic layers are embedded onto a semi-infinite substrate. An embedding potential, derived from the substrate Green function, is added to the Hamiltonian for the surface region, which can then be solved by conventional surface band-structure techniques—such as the linear augmented-plane-wave (LAPW) method used here. The resulting method has the accuracy of the full-potential LAPW method, without the disadvantages associated with the slab and slab-superlattice geometries. Results are presented for Al(001) and Ni(001) surfaces.

I. INTRODUCTION

In this paper we describe a new, self-consistent method for determining surface electronic structure. With this technique we treat the surface of a semi-infinite crystal instead of the usual slab or slab superlattice. Such a treatment is important for experiments such as angle-resolved photoemission and inverse photoemission spectroscopies which probe the spectrum of electronic states; these states can be very different in a slab from those of a semi-infinite system. Moreover, our method concentrates on the actual surface region and provides an economical way of calculating the self-consistent electronic structure.

The difficulty in solving the Schrödinger equation at a surface comes from the breakdown of bulk periodicity perpendicular to the surface. However, the region in which the potential differs significantly from the bulk is confined to a few atomic layers near the surface (at least in a metal). Wave-function matching techniques have taken advantage of this fact by connecting wave functions from the perfect, three-dimensional solid to those in vacuum across the surface region. Lang and Kohn used such a method in their pioneering jellium calculations where the surface was represented by the boundary of a semi-infinite background of uniform positive charge.[1] Corrections due to the lattice can be included by treating the pseudopotential as a perturbation to first order. Reasonable work functions and surface energies can be obtained in this way for s-p-bonded metals; but the jellium model (essentially a one-dimensional model) cannot be used to find the three-dimensional character of the charge density, nor can it be used in the case of transition metals with tightly bound d bands. Appelbaum and Hamann have formulated a general wave-function matching method in which the wave functions are matched by means of a transfer matrix in the surface region.[2] Difficulty is encountered with the implementation of this approach because of the continua of bulk states to be matched, and because the evanescent waves (allowed near the surface region) are usually neglected.

Calculations of surface electronic structure are now dominated by methods which treat a slab of finite thickness, thus avoiding the problem of the semi-infinite substrate. The accurate basis-set methods which have been developed for bulk electronic structure can then be used with relatively little modification. Calculations based on either the slab or slab-superlattice geometries have enjoyed many successes in surface studies; and properties such as work functions, charge densities, potentials, total energies, and spin densities have been accurately determined. However, certain shortcomings are apparent in the geometries themselves, which limit the accuracy of the various methods, regardless of how well they treat the electrostatic or exchange-correlation potentials. Both slab and slab-superlattice geometries force a surface to be located in the vicinity of another surface. In the superlattice a surface may interact with other surfaces both across the vacuum region *and* across the finite width of the slab. In slabs, the two surfaces interact through the (few) atomic layers. These interactions are sizable enough to split the surface states arising from a single surface into hybridized pairs. In aluminum the splitting is nearly 1 eV, even when the slab is nine layers thick.[3] Although this problem is more acute in nearly-free-electron metals, it persists in transition metals by splitting the nonlocalized Shockley states. Another problem with these geometries is the absence of true bulk states. The bulk is only crudely represented by the interior layers of each slab. Bulk energy-band continua existing at each wave vector parallel to the surface are condensed into only a few discrete states, making identification of surface states and surface resonances fairly arbitrary. Also, the requirement that slabs be thick enough to reasonably separate the surfaces makes these calculations computationally expensive, so that only the simplest clean surfaces and overlayer coverages can be studied.

Our approach is to add to the Hamiltonian for the surface region and embedding potential which can describe the influence of the bulk substrate exactly.[4,5] The finite surface region is treated explicitly, and the surface wave functions are forced by the embedding potential to have the correct logarithmic derivatives on the interface with the bulk region. By including, through the embedding potential, the propagation of the wave functions into the bulk we accurately describe both discrete surface states and the bulk continuum. The short metallic screening length means that we need only include a very few layers of atoms in the surface region for explicit calculation, making the method economical, and freeing up computer resources to make possible the study of more complex surfaces and overlayers.

We have previously published a brief report on Al(001) using the present surface embedded Green function (SEGF) method.[6] We now describe the method and some results in detail. Section II and the appendixes present an overview of the embedding method and include the additional terms in the secular equations, the form of basis set [linear augmented plane waves (LAPW)] which we employ, and the matrix-element expressions. We show in Sec. III how we obtain the charge density, electrostatic potential, and exchange-correlation potential from the calculated surface Green function. In Secs. IV and V we present our self-consistent results for the Al(001) and Ni(001) surfaces along with studies of convergence criteria. Discussion and conclusions follow in section VI.

II. THE EMBEDDED SURFACE HAMILTONIAN

A. The embedding method

The embedding method is based on a variational principle in which we define a trial function $\phi(\mathbf{r})$ only in the region of space we want to treat explicitly—the surface region (region I in Fig. 1). This wave function is extended into the substrate (region II—the bulk crystal) with an exact solution ψ of the bulk Schrödinger equation at some energy ε, which matches onto ϕ in amplitude over the interface S between regions I and II. The expectation value of the Hamiltonian with ϕ in I and ψ in II is then given (in atomic units, with $e=\hbar=m=1$) by

$$E=\frac{\int_{\mathrm{I}} d^3\mathbf{r}\,\phi^* H\phi+\varepsilon\int_{\mathrm{II}} d^3\mathbf{r}\,|\psi|^2+\frac{1}{2}\int_S d^2\mathbf{r}_S\phi^*\frac{\partial\phi}{\partial n_S}-\frac{1}{2}\int_S d^2\mathbf{r}_S\phi^*\frac{\partial\psi}{\partial n_S}}{\int_{\mathrm{I}} d^3\mathbf{r}\,|\phi|^2+\int_{\mathrm{II}} d^3\mathbf{r}\,|\psi|^2}\ . \tag{1}$$

The surface integrals in (1) come from the discontinuity in the derivative $\partial\phi/\partial n_S$ and $\partial\psi/\partial n_S$ across interface S. The fundamental principle of embedding is that the integrals through the substrate in Eq. (1) can be eliminated, provided that the Green function for the perfect crystal can be found, subject to the boundary condition on interface S that

$$\frac{\partial G_0(\mathbf{r}_S,\mathbf{r}')}{\partial n_S}=0\ . \tag{2}$$

The inverse of G_0 over S is a generalized logarithmic derivative, relating the derivative of a solution of the Schrödinger equation in II to the amplitude:

$$\frac{\partial\psi(\mathbf{r}_S)}{\partial n_S}=-2\int_S d^2\mathbf{r}'_S\,G_0^{-1}(\mathbf{r}_S,\mathbf{r}'_S)\psi(\mathbf{r}'_S)\ . \tag{3}$$

Substituting (3) in (1) and making use of a relationship between normalization integrals in II and the energy derivative of $\partial\psi/\partial n_S$,[4] we may write

$$E=\frac{\int_{\mathrm{I}} d^3\mathbf{r}\,\phi^* H\phi+\frac{1}{2}\int_S d^2\mathbf{r}_S\phi^*\frac{\partial\phi}{\partial n_S}+\int_S d^2\mathbf{r}_S\int_S d^2\mathbf{r}'_S\phi^*(\mathbf{r}_S)\left[G_0^{-1}-\varepsilon\frac{\partial G_0^{-1}}{\partial E}\right]\phi(\mathbf{r}'_S)}{\int_r d^3\mathbf{r}\,|\phi|^2-\int_S d^2\mathbf{r}_S\int_S d^2\mathbf{r}'_S\,\phi^*(\mathbf{r}_S)\dfrac{\partial G_0^{-1}}{\partial E}\phi(\mathbf{r}'_S)}\ . \tag{4}$$

This variational expression for the energy depends explicitly only on ϕ in region I, with G_0^{-1} evaluated over S containing all the information about the substrate.

To minimize E, let us expand ϕ in terms of a set of basis functions:

$$\phi(\mathbf{r})=\sum_i a_i\chi_i(\mathbf{r})\ . \tag{5}$$

We then obtain a matrix equation for the coefficients a_i:

$$\sum_j\left[H_{ij}+(G_0^{-1})_{ij}+(E-\varepsilon)\frac{\partial(G_0^{-1})_{ij}}{\partial E}\right]a_j=E\sum_j O_{ij}a_j\ , \tag{6}$$

where

$$H_{ij}=\int_{\mathrm{I}} d^3\mathbf{r}\,\chi_i^*(\mathbf{r})H\chi_j(\mathbf{r})+\frac{1}{2}\int_S d^2\mathbf{r}_s\chi_i^*\frac{\partial\chi_j}{\partial n_S}\ ,$$
$$(G_0^{-1})_{ij}=\int_S d^2\mathbf{r}_S\int_S d^2\mathbf{r}'_S\chi_i^*(\mathbf{r}_S)G_0^{-1}(\mathbf{r}_S,\mathbf{r}'_S)\chi_j(\mathbf{r}'_S)\ , \tag{7}$$

and

$$O_{ij}=\int_I d^3\mathbf{r}\,\chi_i^*(\mathbf{r})\chi_j(\mathbf{r})\ .$$

H_{ij} is the matrix element of the Hamiltonian in region I, with an additional surface integral which ensures Hermiticity. $(G_0^{-1})_{ij}$ is the matrix element of G_0^{-1}—*the embedding potential*—converting the calculation for region I into a calculation for I joined onto the substrate II. The energy-derivative term, entering (4) from the normalization of the wave function in the substrate, gives a first-order correction so that G_0^{-1} is evaluated at the right energy. G_0^{-1} is in fact a *pseudopotential,* describing the scattering of the electrons incident on the substrate from region I. The relationship between the energy derivative of G_0^{-1} and the normalization integrals through region II is identical to that for an ordinary pseudopotential, between its energy derivative and the "orthogonality hole" in the atomic core.

Normally we calculate the Green function for the surface region, which we can similarly expand in terms of our basis functions:

$$G(\mathbf{r},\mathbf{r}';E)=\sum_{i,j} g_{ij}(E)\chi_i(\mathbf{r})\chi_j^*(\mathbf{r}')\ , \tag{8}$$

where g_{kj} satisfies

$$\sum_k [H_{ik}+(G_0^{-1})_{ik}-EO_{ik}]g_{kj}(E)=\delta_{ij}\ ; \tag{9}$$

and by evaluating the embedding potential G_0^{-1} at the energy E at which we are working, the energy-derivative terms in (6) disappear. From the Green function we can find the surface density of states and the charge density (see Sec. III).

B. The embedding potential

The interface between the surface region and the substrate might be taken as surface S in Fig. 1, weaving its way between the muffin-tin (MT) spheres. However, it would be difficult to evaluate the matrix-element integrals in this awkwardly shaped region I. It is, in fact, possible to transfer G_0^{-1} from surface S to a more convenient flat surface S_0, with a constant potential in between (Fig. 1). This follows from the properties of the embedding variational principle (4): by varying ϕ we can show that E is stationary when

$$H\phi=E\phi \text{ in region I} \tag{10}$$

and

$$\partial\phi(\mathbf{r}_S)/\partial n_S=-2\int_S d^2\mathbf{r}'_S[G_0^{-1}-(E-\varepsilon)\partial G_0^{-1}/\partial E]\phi(\mathbf{r}'_S)\ . \tag{11}$$

Not only must ϕ satisfy the Schrödinger equation in region I, but it must also have the right logarithmic derivative on S. Now, given a logarithmic derivative on S, we can integrate the Schrödinger equation through the constant potential to surface S_0 to find a new logarithmic derivative which we call $\tilde{G}_0^{-1}$. If we now minimize (4) with $\tilde{G}_0^{-1}$ substituted for G_0^{-1}, and extend region I right up to the plane S_0, we obtain a wave function ϕ which satisfies (10). Because it has a logarithmic derivative $\tilde{G}_0^{-1}$ on S_0, it must have logarithmic derivative G_0^{-1} on S; thus, it is the solution we require.

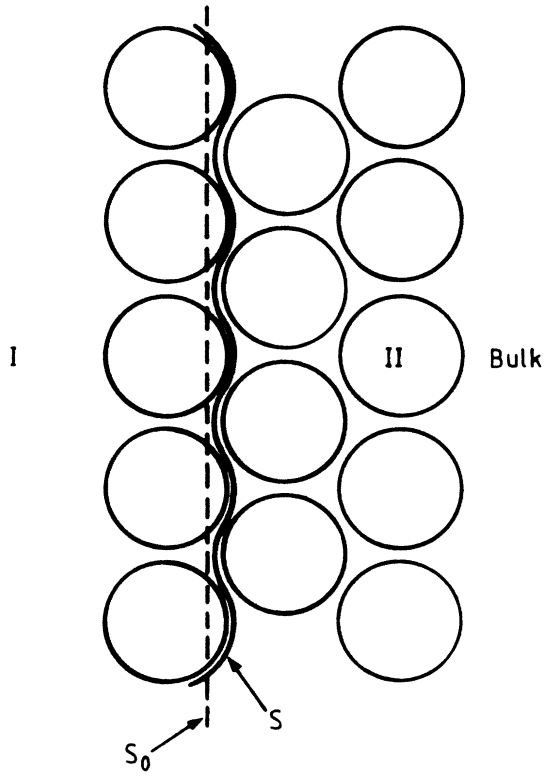

FIG. 1. The surface region I is separated from the substrate region II by a complicated interface S. However, an effective embedding interface S_0 can be defined.

The embedding potential is directly related to the reflection properties of the perfect crystal. First let us use the two-dimensional Bloch properties of the wave functions so that the embedding potential at wave vector $\mathbf{K}$ can be expanded over S_0 in a Fourier series (we drop the tilde on $\tilde{G}_0^{-1}$):

$$G_{0,\mathbf{K}}^{-1}(\mathbf{R},\mathbf{R}')=\frac{1}{A}\sum_{m,m'} G_{0,\mathbf{K}}^{-1}(m,m')\times\exp[i(\mathbf{K}_m\cdot\mathbf{R}-\mathbf{K}_{m'}\cdot\mathbf{R}')]\ , \tag{12}$$

where

$$\mathbf{K}_m=\mathbf{K}+\mathbf{G}_m\ .$$

$\mathbf{R}$ is the component of $\mathbf{r}$ parallel to the surface, $\mathbf{G}_m$ is a surface reciprocal-lattice vector, and A is the area of the surface unit mesh. We now truncate the perfect crystal at S_0, with a constant potential continued to the left. If a plane wave $\exp(i\mathbf{K}_m\cdot\mathbf{R})\exp(ik_z z)$ is incident on the crystal, it will be scattered, and the total wave function to the left of S can be written as

$$\psi(\mathbf{r})=\exp(i\mathbf{K}_m\cdot\mathbf{R})\exp(ik_z z)+\sum_{m'}R_{m',m}\exp(i\mathbf{K}_{m'}\cdot\mathbf{R})\exp(\gamma_{m'}z)\ ,$$

where R is the reflection matrix and $K_{m'}^2-\gamma_{m'}^2=K_m^2+k_z^2$. The Fourier coefficients of ψ and $\partial\psi/\partial n_S$ on S are then given by

$$\begin{aligned}\psi_{m'}&=\delta_{m',m}+R_{m',m}\ ,\\ \psi'_{m'}&=\gamma_{m'}(-\delta_{m',m}+R_{m',m})\ .\end{aligned}\tag{13}$$

So by inverting Eq. (3) we find that $G_{0,\mathbf{K}}^{-1}$ is given by

$$G_{0,\mathbf{K}}^{-1}=\tfrac{1}{2}\gamma(1-R)(1+R)^{-1}\ .\tag{14}$$

At the present time we determine R, and thus G_0^{-1}, using a muffin-tin potential in the substrate. The layer-doubling method, described by Pendry and used in low-energy electron diffraction (LEED) and photoemission calculations, provides a simple way of determining R with this form of potential.[7] The crystal is divided up into layers, and multiple-scattering techniques are used to determine the reflection and transmission properties of a single layer. These can be used to find the reflection and transmission properties of a pair of layers and the process repeated to 4,8,. . . layers. With a small imaginary part to the energy, this process converges rapidly to give the reflection matrix R for the semi-infinite substrate. It is not a serious approximation to use the MT potential in the substrate, provided the band structure is good. The short screening length ensures that deficiencies in the substrate potential do not propagate far into the surface region, where we use the full potential without shape approximations.

The embedding potential does not depend on the potential in region I, and it can be tabulated once for all, over the energy mesh at which we intend to determine the surface Green function G [see Eq. (8)]. Typically we find that 13-surface reciprocal-lattice vectors are adequate for expanding G_0^{-1} in the fairly close-packed surfaces we have studied.

C. LAPW basis functions and matrix elements

LAPW's provide an accurate and convenient basis for the wave functions or Green function in region I. As in conventional slab calculations,[8] these are constructed by dividing space into three regions: the interstitial region—where the potential is relatively flat, muffin-tin (MT) spheres around each atom—where the major component of the potential is spherically symmetric, and the vacuum region—where the potential has a strong z dependence, but a relatively weak x and y dependence. In the interstitial region the LAPW's are plane waves of the from

$$\left.\begin{matrix}\chi_{m,n}^{+}(\mathbf{r})\\ \chi_{m,n}^{-}(\mathbf{r})\end{matrix}\right\}=\sqrt{2/\Omega}\exp(i\mathbf{K}_m\cdot\mathbf{R})\times\begin{cases}\cos(k_n z), & n \text{ even}\ ,\\ \sin(k_n z), & n \text{ odd}\ ,\end{cases}\tag{15a,15b}$$

where

$$k_n=n\pi/\tilde{D}\ ,$$

with n even for the symmetric case $(+)$ and n odd for the antisymmetric case $(-)$ under the reflection $z\rightarrow -z$, and

$$\Omega=AD\ .$$

D is the film thickness and $\tilde{D}$ $(>D)$ defines the wave vectors perpendicular to the surface. Inside the MT spheres the LAPW is composed of radial functions $u_{l,\alpha}$ and energy derivatives $\dot{u}_{l,\alpha}$—solutions of the scalar relativistic equation with the spherically symmetric part of the atomic potential at an energy parameter $E_{l,\alpha}$:

$$\left.\begin{matrix}\chi_{m,n}^{+}(\mathbf{r})\\ \chi_{m,n}^{-}(\mathbf{r})\end{matrix}\right\}=\sum_L\left[\begin{Bmatrix}A_{L,\alpha}^{+}(\mathbf{K})\\ A_{L,\alpha}^{-}(\mathbf{K})\end{Bmatrix}\times u_{l,\alpha}+\begin{Bmatrix}B_{L,\alpha}^{+}(\mathbf{K})\\ B_{L,\alpha}^{-}(\mathbf{K})\end{Bmatrix}\times\dot{u}_{l,\alpha}\right]Y_L(\Omega)\times\begin{cases}i^l & \text{(16a)}\\ i^{l-1}\ . & \text{(16b)}\end{cases}$$

We normally go up to $l=8$ in this expression. The A and B coefficients are determined by matching χ and its radial derivative across the surface of the MT spheres (see Appendix A). Finally, in the vacuum region we solve the Schrödinger equation with the planar-averaged part of the potential at some energy E_v to give a z dependent function $v_m(z)$ and its energy derivative $\dot{v}_m(z)$. The LAPW in this region is a linear combination of these and a two-dimensional plane wave:

$$\chi_{m,n}^{\pm}(\mathbf{r})=[\alpha^{\pm}(m,n)v_m(z)+\beta^{\pm}(m,n)\dot{v}_m(z)]\exp(i\mathbf{K}_m\cdot\mathbf{R})\ .\tag{17}$$

The α and β coefficients are chosen so that χ and $\partial\chi/\partial z$ are continuous at the vacuum-slab boundary (see Appendix A).

Since they contain $u,\dot{u}$ inside the atom, and $v,\dot{v}$ in the vacuum region, the LAPW's can represent an accurate solution of the wave equations in these regions over a considerable range about the parametrized energies $E_{l,\alpha}$ and E_v. The plane waves also provide a rapidly convergent representation of the wave functions in the interstitial region, where the potential only varies relatively slowly. The choice of $\tilde{D}$ is, to some extent, arbitrary. It should be somewhat larger than D to give the plane waves in Eq. (15) a range of matching conditions onto the vacuum solutions (17). Moreover, we require a range of logarithmic derivatives on the embedding plane at S_0. We shall discuss this in detail in Sec. IV A. With the embedding surface shifted to S_0, halfway between atomic planes (see Fig. 2), caps of the surface muffin-tin spheres are apparently chopped off. Actually, the contribution of

the entire muffin-tin potential to the surface Hamiltonian is included, and only the interstital contribution with the flat potential between S and S_0 is modified.

Although the basis functions are constructed by dividing region I into the film muffin-tin form, the matrix elements are evaluated with the *full* potential. This is expressed in the interstitial region in the form

$$V(\mathbf{r})=\sum_{m,n} V_{m,n}\exp(i\mathbf{G}_m\cdot\mathbf{R})\times\begin{Bmatrix}\cos(k_n z)\\ \sin(k_n z)\end{Bmatrix}+V_1 z+V_2 z^2+\sum_{m\ (\neq 0)}[V_{m+}\exp(G_m z)+V_{m-}\exp(-G_m z)]\exp(i\mathbf{G}_m\cdot\mathbf{R})\ . \tag{18}$$

The $V_{m,n}$ are Fourier coefficients in an expansion over surface reciprocal-lattice vectors $\mathbf{G}_m$ and wave vectors k_n, as in Eq. (15). The remaining terms come from the solution of Poisson's equation in our surface geometry (see Sec. III B). Inside the MT spheres we expand V in spherical harmonics:

$$V(\mathbf{r})=\sum_L V_L(r)Y_L(\theta,\varphi)\ , \tag{19}$$

where the collective angular-momentum index $L=\{l,m\}$. In the vacuum region we have the partial Fourier expansion

$$V(\mathbf{r})=\sum_m V_m(z)\exp(i\mathbf{G}_m\cdot\mathbf{R})\ . \tag{20}$$

The matrix elements of the kinetic-energy operator, plus the muffin-tin part of the potential [the spherically symmetric part of Eq. (19)], and the $m=0$ term in (20) can be found in a straightforward manner, the results being outlined in the Appendixes. The addition of the matrix element of the normal derivative (7) ensures Hermiticity. The matrix elements of each term in (18) through the interstitial region can also be evaluated analytically, apart from correction terms when MT spheres protrude through the embedding plane (see Appendix C). Finally, the matrix elements of the remaining parts of (19) and (20) must be evaluated numerically; for the MT region this is quite time consuming, since the potential and the wave functions all involve separate summations over l,m.

The matrix element of the embedding potential is trivial with LAPW basis functions:

$$\langle\chi_{m',n'}\,|\,G_0^{-1}\,|\,\chi_{m,n}\rangle=\frac{2}{D}\begin{Bmatrix}\cos(k_{n'}\zeta)\\ \sin(k_{n'}\zeta)\end{Bmatrix}\times(G_0^{-1})_{m,m'}\begin{Bmatrix}\cos(k_n\zeta)\\ \sin(k_n\zeta)\end{Bmatrix}\ , \tag{21}$$

where ζ is the z coordinate of the embedding surface S_0 (Fig. 2). If m or m' exceeds the maximum reciprocal-lattice vector in the expansion for G_0^{-1}, the matrix element is set equal to its free-electron value, without significant loss of accuracy. This term is the only energy-dependent part of the Hamiltonian, so it is very easy to determine the Green function G, Eqs. (8) and (9), over any energy range required.

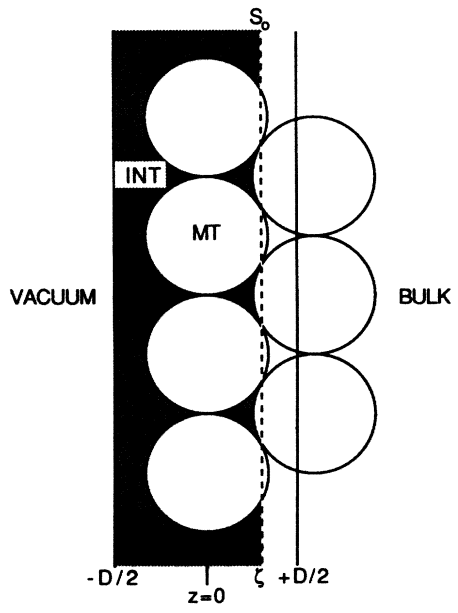

FIG. 2. The interstitial, muffin-tin, vacuum, and bulk regions. When taken to be halfway between atomic planes, the embedding interface S_0 slices through surface and bulk muffin tins.

III. SELF-CONSISTENT CHARGE DENSITY AND POTENTIAL

A. The charge density

The local density of states $\sigma(\mathbf{r},E)$—the charge density of electrons at a particular energy—can be found immediately from the Green function given by (8) and (9):

$$\sigma(\mathbf{r},E)=\sum_i |\psi_i(\mathbf{r})|^2\delta(E-E_i)$$
$$=\frac{1}{\pi}\mathrm{Im}G(\mathbf{r},\mathbf{r};E+i\epsilon)\ . \tag{22}$$

By integrating σ over the occupied states, we can then find the charge density $\rho(\mathbf{r})$. The integral is most economically evaluated by contour integration, making use of the analyticity of G in the upper half plane. We use a semicircular contour, starting off at some energy below the bottom of the valence band, and finishing back on the real axis at the bulk Fermi energy:

$$\rho(\mathbf{r})=\frac{1}{\pi}\mathrm{Im}\int dE\, G(\mathbf{r},\mathbf{r};E) \text{ with the semicircle in the upper half plane .} \tag{23}$$

Even if the density of states is structured along the real axis, G varies smoothly along the contour except where it approaches structure along the real axis at E_F. Gauss-Chebychev provides a good numerical technique for carrying out the integration, particularly since it concentrates the sampling points near the ends of the range—just where significant structure may appear in the integrand. We find that 15–31 sampling points are adequate, except for metals such as Ni where there is a peak in the density of states at E_F. In these cases we use 63 sampling points. In comparing timings of this embedding method with slab calculations, this represents the number of matrix inversions for evaluating the Green function, independent of the size of the system. In a slab calculation, a single matrix diagonalization is required to find the discrete eigenvalues, but the number of eigenstates scales with the size.

In addition to the integral over energy, we must sum over wave vectors $\mathbf{K}$ in the surface Brillouin zone. Here we sample at the special $\mathbf{K}$ points given by Cunningham.[9] Typically we use 10 points in the irreducible part of the surface BZ, using symmetry to determine the contribution to the charge density of equivalent parts of the zone. Problems might be encountered in this special point sampling is sharp features (such as surface states or resonances) cross the Fermi energy—in other words, the sampling of partly filled bands. The remedy in such cases is simply to increase the number of $\mathbf{K}$ points.

The charge density itself is reexpanded in the same form as the potential:

$$\rho(r)=\begin{cases}\displaystyle\sum_{m,n}\rho_{mn}\exp(i\mathbf{G}_m\cdot\mathbf{R})\times\begin{Bmatrix}\cos(k_n z)\\ \sin(k_n z)\end{Bmatrix}, & \text{with r in the interstitial region ,} \quad (24a)\\ \displaystyle\sum_{L}\rho_L Y_L(\theta,\varphi), & \text{with r in MT spheres ,} \quad (24b)\\ \displaystyle\sum_{m}\rho_m(z)\exp(i\mathbf{G}_m\cdot\mathbf{R}), & \text{with r in vacuum .} \quad (24c)\end{cases}$$

As in other applications of the LAPW method, $l=8$ is sufficient in the spherical-harmonic expansion. These reexpansions are relatively easy to evaluate from the double expansion of the Green's function, Eqs. (8), (15), and (17). To Eq. (24) is added the charge density of the core levels, which we find by solving the Dirac equation in the spherical part of the atomic potentials.

An important difference between the SEGF method and slab calculations is that here the occupation of states is determined by the *bulk Fermi energy,* whereas in slab calculations it is determined by the total number of electrons in the finite system. This means that the surface region is not constrained to be charge neutral, and that the total number of electrons in the whole system (surface + substrate) is not automatically conserved. In fact, the process of self-consistency (Sec. III B) ensures that the surface is almost neutral. If our assumption is correct that the potential beyond the embedding plane is nearly the same as in the bulk, the total number of electrons will be almost exactly conserved. For studies of work function and surface electronic structure this is all that is required. However, it is straightforward to achieve *exact* conservation of the number of electrons by adding a small, constant potential to the Hamiltonian in region I: this represents the potential produced by any residual transfer of electrons between regions I and II. The total number of electrons in the system can be found from a generalized surface phase shift,[10] given in terms of the embedded surface Hamiltonian, and we shall give an example of this in Sec. IV C.

B. The potential

Because the surface geometry differs from that in slab calculations, the method of determining the potential must be modified. The electrostatic potential must now be found by solving Poisson's equation subject to the boundary conditions that there is no electric field as z tends to $-\infty$ (the total system is neutral at self-consistency), and the potential matches to the bulk potential on the interface with the substrate.

The first stage of calculating the electrostatic potential is to find the Fourier expansion of a pseudo-charge-density $\tilde{\rho}$ extended through the whole region between $-D/2$ and $+D/2$ (Fig. 2). We require that $\tilde{\rho}=\rho$ in the interstitial region, and that $\tilde{\rho}$ have the same multipole moments as the actual charge density inside the muffin-tin spheres. We then solve Poisson's equation with $\tilde{\rho}$ throughout this region while ignoring the MT spheres. Next, the potential inside the spheres can be found by solving Poisson's equation with the actual MT charge, subject to the boundary condition that the potential match the known value at the MT-sphere boundary. First, we extend the Fourier expansion of ρ, Eq. (24), into the spheres, and subtract off this term within the spheres:

$$\rho(\mathbf{r})=\sum_{m,n}\rho_{mn}\exp(i\mathbf{G}_m\cdot\mathbf{R})\times\begin{Bmatrix}\cos(k_n z)\\ \sin(k_n z)\end{Bmatrix}$$
$$+\sum_{\alpha}\Theta(r-r_{\mathrm{MT},\alpha})\left[\sum_{L}\rho_L Y_L(\theta,\varphi)-\sum_{m,n}\rho_{mn}\exp(i\mathbf{G}_m\cdot\mathbf{R})\times\begin{Bmatrix}\cos(k_n z)\\ \sin(k_n z)\end{Bmatrix}\right] \text{ for } |z|<D/2 . \tag{25}$$

Here Θ is a step function equal to 1 if $\mathbf{r}$ is inside the MT sphere α, and zero otherwise. We can then write

$$\tilde{\rho}(\mathbf{r})=\sum_{m,n}\rho_{mn}\exp(i\mathbf{G}_m\cdot\mathbf{R})\times\begin{Bmatrix}\cos(k_n z)\\ \sin(k_n z)\end{Bmatrix}+\sum_{\alpha}\rho_{\text{pseudo},\alpha}(\mathbf{r})\ , \tag{26}$$

where $\rho_{\text{pseudo},\alpha}$ is a charge density lying within muffin-tin α with the same multipole moments as the expression in square brackets in Eq. (25). Weinert has shown how to construct a convenient form of $\rho_{\text{pseudo},\alpha}$ which can be readily Fourier transformed.[11]

We now work with $\tilde{\rho}(\mathbf{r})$, which we expand as

$$\tilde{\rho}(\mathbf{r})=\sum_{m,n}\tilde{\rho}_{mn}\exp(i\mathbf{G}_m\cdot\mathbf{R})\times\begin{Bmatrix}\cos(k_n z)\\ \sin(k_n z)\end{Bmatrix}\ . \tag{26'}$$

The general solution of Poisson's equation, the electrostatic charge density $V^{\text{es}}(\mathbf{r})$, corresponding to this charge density, is given by

$$V^{\text{es}}(\mathbf{r})=A+\sum_{m,n}{}'\frac{4\pi\rho_{m,n}}{G_m^2+k_n^2}\exp(i\mathbf{G}_m\cdot\mathbf{R})\times\begin{Bmatrix}\cos(k_n z)\\ \sin(k_n z)\end{Bmatrix}+Bz$$

$$-2\pi\rho_{0,0}z^2+\sum_{m}{}'[V_{m+}\exp(G_m z)+V_{m-}\exp(-G_m z)]\exp(i\mathbf{G}_m\cdot\mathbf{R})\ , \tag{27}$$

where A, B, V_{m+}, and V_{m-} are fitted to the boundary conditions, as described below.

In the vacuum region we solve Poisson's equation with the charge density expressed in the form

$$\rho(\mathbf{r})=\sum_{m}\rho_m(z)\exp(i\mathbf{G}_m\cdot\mathbf{R})\ . \tag{28}$$

For each Fourier component the electrostatic potential satisfies

$$\frac{d^2V_m^{\text{es}}(z)}{dz^2}+G_m^2V_m^{\text{es}}(z)=4\pi\rho_m(z)\ , \tag{29}$$

which we solve subject to the boundary condition that $V^{\text{es}}(\mathbf{r})$ goes to a constant, with zero electric field, as $z\rightarrow-\infty$. This leaves solutions of the homogeneous equation in the vacuum region, $C+\sum_m' V_m^{\text{hom}}\exp(G_m z)$, which must be fitted by boundary conditions at $z=-D/2$, the interface between the vacuum and the slab. These conditions, that V^{es} and $\partial V^{\text{es}}/\partial z$ are continuous, give two equations for each Fourier component parallel to the surface. However, for each $\mathbf{G}_m$ there are three unknowns: A, B, and C for $\mathbf{G}_m=\mathbf{0}$ and V_{m+}, V_{m-}, and V_m^{hom} for nonzero $\mathbf{G}_m$. The additional boundary condition comes from the continuity in V^{es} at the interface between the surface and substrate. The bulk electrostatic potential at random points on the interface is read in and a least-squares fit is performed to fully determine all constants in the potential.

Our expression for the electrostatic potential in the interstitial region now has the same form as in Eqs. (18) and (20). We leave the linear, quadratic, and exponential terms explicitly in (18), instead of Fourier transforming them, avoiding errors arising from a finite expansion. The expression for the electrostatic potential is valid over the surface of the muffin-tin spheres, providing us with the required boundary condition for integrating Poisson's equation within each sphere. This gives us the potential expanded in the form

$$V^{\text{es}}(\mathbf{r})=\sum_{L}V_L^{\text{es}}(r)Y_L(\Omega)\ . \tag{30}$$

To the electrostatic potential we add the exchange-correlation potential, in the local density approximation, to construct the total one-electron potential. We have found it sufficient in the MT sphere and vacuum regions to use two terms in a Taylor series expansion:

$$V^{\text{xc}}(\rho(\mathbf{r}))=\begin{cases}V^{\text{xc}}(\rho_{00}(r)/\sqrt{4\pi})+\sum_{L}{}'\dfrac{dV^{\text{xc}}}{d\rho}(\rho_{00}(r)/\sqrt{4\pi})\rho_L Y_L(\theta,\phi), & \text{with } \mathbf{r} \text{ in MT spheres}\ , \quad (31a)\\ V^{\text{xc}}(\rho_0(z))+\sum_{m}{}'\dfrac{dV^{\text{xc}}}{d\rho}(\rho_0(z))\rho_m(z)\exp(i\mathbf{G}_m\cdot\mathbf{R}), & \text{with } \mathbf{r} \text{ in vacuum}\ . \quad (31b)\end{cases}$$

The mean-square error in these expansions is of the order of 10^{-4} hartree. In the interstitial region the Taylor series expansion is not sufficiently accurate; so, instead, we do a least-squares fit of typically 100 points to 50 star-of-**k** functions. The root-mean-square error in this procedure is about 3×10^{-4} hartrees.

IV. Al(001) RESULTS

A. Convergence criteria

To test the convergence of the SEGF method we examine first a non-self-consistent calculation of the Al(001) charge density, comparing results with one and two lay-

ers treated explicitly in the surface region. The embedding plane is taken halfway between atomic layers to treat surface and substrate on an equal footing. The thickness D of the embedded single-layer slab is 5.374 a.u. Taking $\tilde{D}$ as either 6 or 7 a.u. with 60 LAPW's gives similar results (Figs. 3 and 4). There is, however, some discrepancy on the vacuum side of the slab because $\tilde{D}=6$ a.u., close to D, does not give enough variation in the logarithmic derivative on the vacuum/slab interface at $z=-D/2$. Results with 60 and 80 plane waves, for $\tilde{D}=7$ a.u., are rather close, with only small differences near the effective embedding plane (Figs. 4 and 5). It is interesting to see how the charge density beyond the embedding plane—where it is no longer physical—is simulating the presence of the substrate atoms. In the two-layer calculation, with $D=9.174$ a.u. and $\tilde{D}=12$ a.u., we find that 100 LAPW's give adequate convergence. Since these non-self-consistent calculations use the same potential in the surface and substrate regions, the results for the one- and two-layer calculations should be completely comparable. Comparing Figs. 5 and 6 we see excellent agreement for the charge density in the surface layer.

A problem in convergence can arise as the number of LAPW's is increased. After apparently converging—in

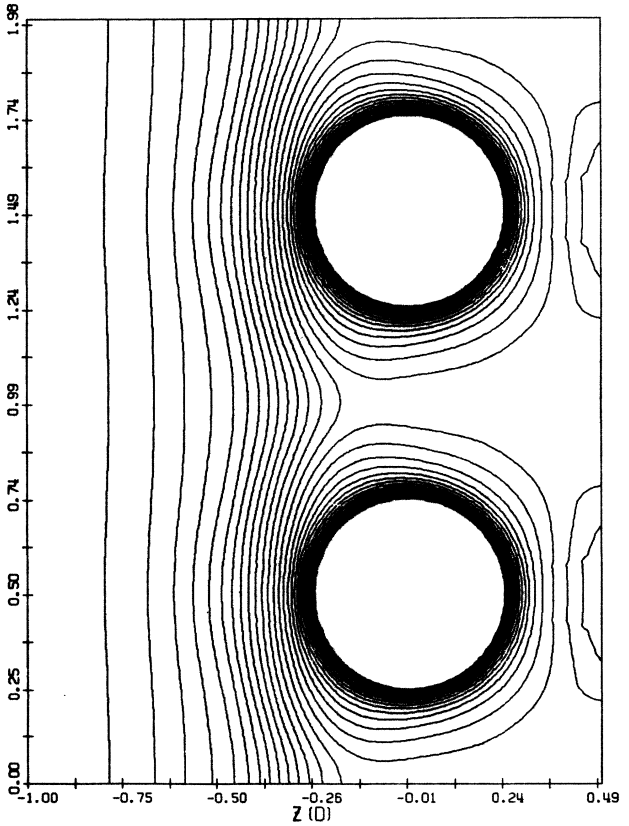

FIG. 3. Single-layer total valence charge density in the (110) bulk Al plane: 60 LAPW's, $\tilde{D}=7$ a.u. (Vacuum is at the left). Lowest contour has $\rho=0.002$ a.u.; successive contours differ by 0.002 a.u. The embedding plane is defined by $z=\zeta=0.35D$.

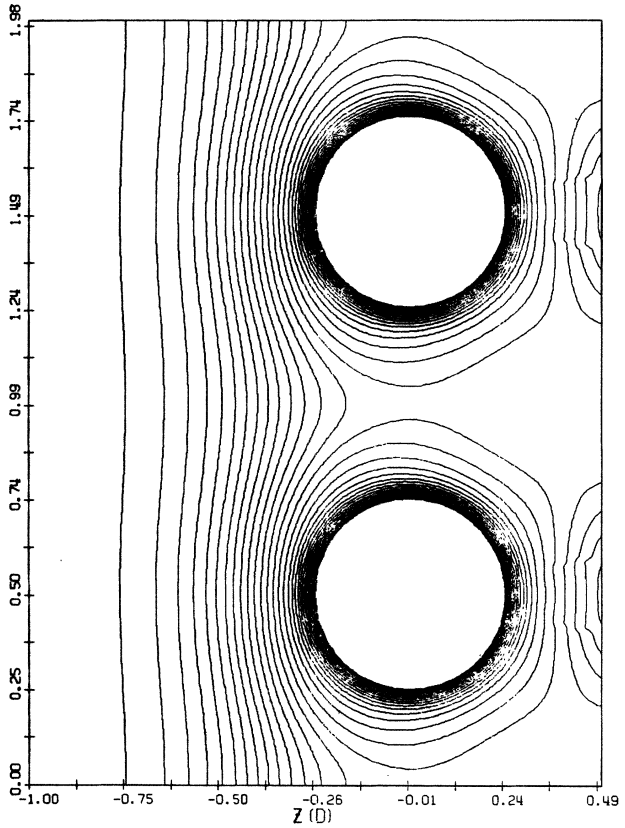

FIG. 4. Same view as in Fig. 3: 60 LAPW's, $\tilde{D}=7$ a.u.

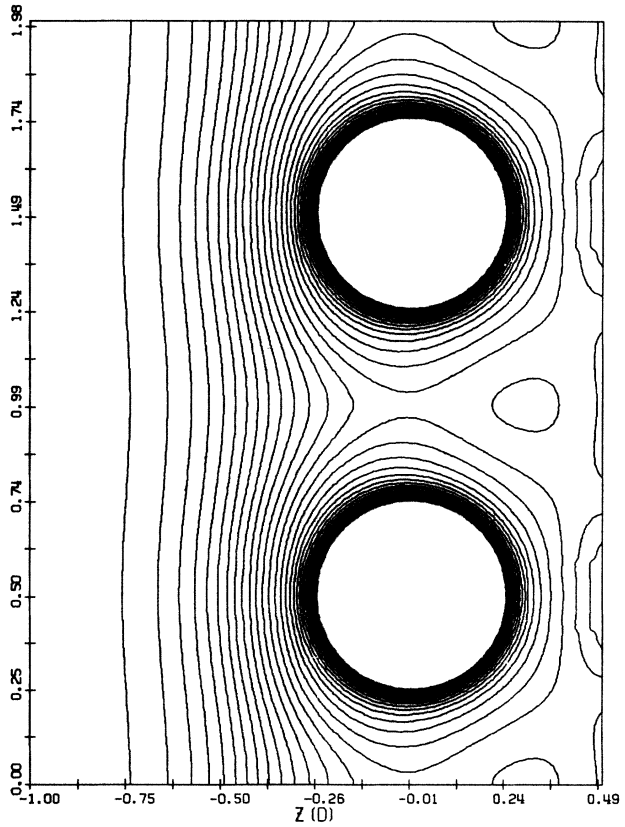

FIG. 5. Same view as in Figs. 3 and 4: 80 LAPW's, $\tilde{D}=7$ a.u.

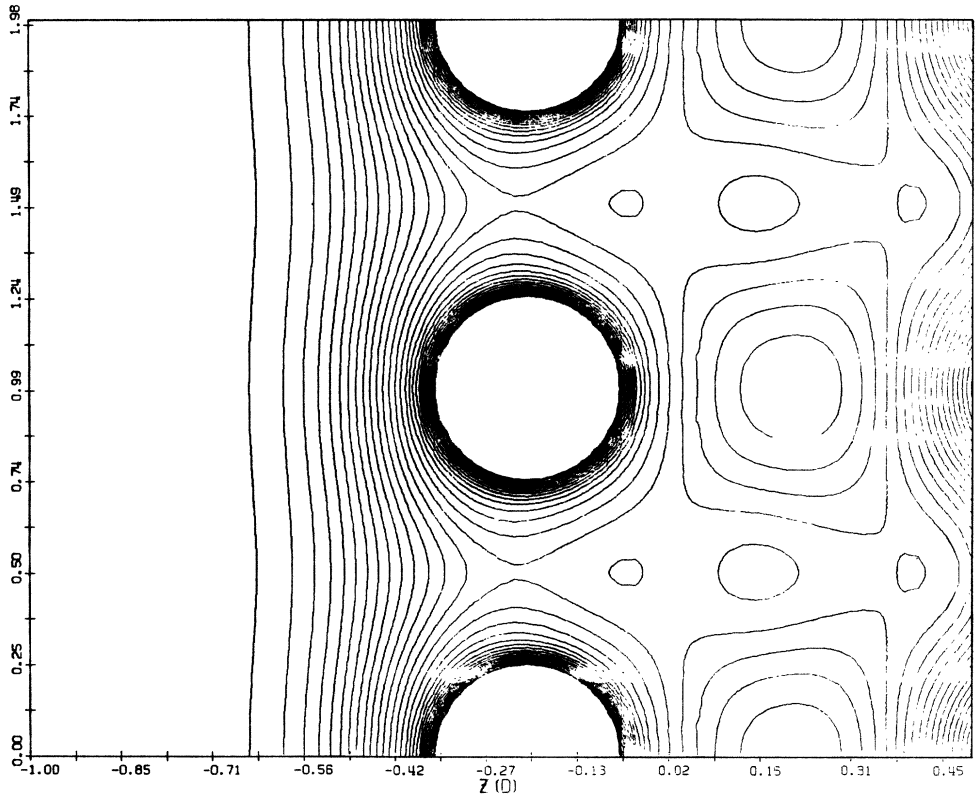

FIG. 6. Double-layer total valence charge density in the (110) bulk Al plane: 100 LAPW's, $\tilde{D}=12$ a.u.

the case of single-layer Al(001) at about 100 plane waves—the results suddenly become nonsensical. However, increasing the number of basis functions restores sensible behavior; and with 120 or more LAPW's, the Al(001) surface density of states and charge density are very close to the results with less than 100. The instability may be associated with the choice of embedding plane—because we effectively require an integration of the Schrödinger equation from the surface of protruding muffin-tins to the plane itself. Using an embedding plane to the bulk side of the muffin-tins, while not as symmetric, eliminates this annoying behavior in most cases.

Most of the parameters in the basis set and the rest of the self-consistent calculation are the same as in conventional LAPW-slab calculations. One important additional parameter is the number of reciprocal lattice vectors used to expand the embedding potential. In the Al work 9–13 reciprocal-lattice vectors are adequate.

B. Work function

The calculated work function for a given surface depends critically on the distribution of charge near the surface. Thus, the agreement between the experimental work function and theory often provides a good indication of the accuracy of the computational method. The most recent work function measurement for Al(001) yielded a value of 4.41 ± 0.03 eV.[12] (An earlier measurement gave 4.2 eV.[13]) Previous theoretical values include 4.2 eV for the jellium model,[1] 5.5 eV for a three-layer slab,[14] 4.7 eV for a nine-layer slab,[15] and 4.53 eV for a nine-layer full-potential LAPW-slab calculation.[16]

We have performed two self-consistent SEGF calculations: one for a single embedded layer of atoms, and one for a double layer. Our calculated work functions are 4.63 and 4.50 eV for the single and double layer, respectively. The difficulty in obtaining an accurate Al(001) work function in slab calculations is probably associated with the discretization of the states in a system of finite thickness. Broad continua of bulk states are crudely represented by a few (discrete) states. This is likely to be a more serious problem in nearly-free-electron metals like aluminum than it would be in transition metals having a large density of *d* states.

Since the SEGF method correctly treats the continua of bulk states through the embedding potential, and also allows the proper decay of surface states into the bulk, it is to be expected that accurate work functions may be obtained with only a few atomic layers. Our double-layer result is closer to experiment than all previous work. Even the *single*-layer work function is superior to all but the *nine*-layer full-potential LAPW. Thus the SEGF method is capable of providing accurate results using a fraction of the computational resources of other methods.

C. Total charge density

Our calculated total charge density for the double layer is displayed in Fig. 7. Charge density contours are in units of valence electrons per bulk unit cell—so the 3.0

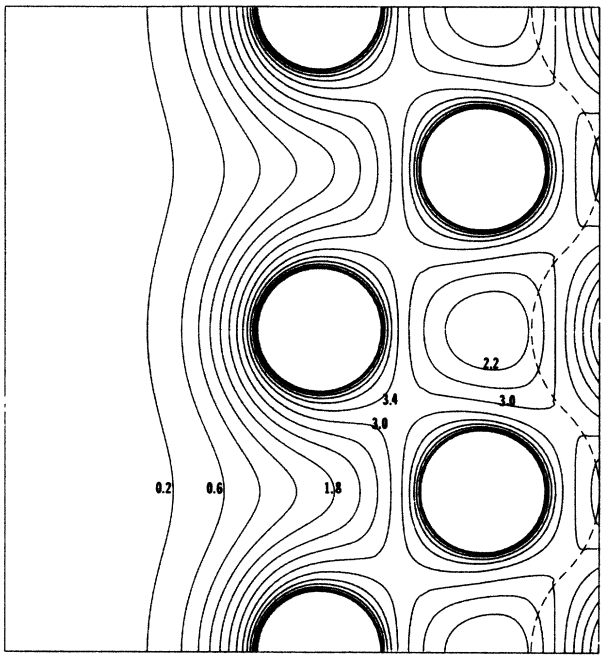

FIG. 7. Self-consistent total valence charge density in the (100) bulk Al plane: 80 LAPW's, $\tilde{D}=12$ a.u. (Vacuum is at the left.) Successive contours differ by 0.4 electrons per bulk unit cell. The dashed curve represents the embedding surface S.

contour should figure prominently in plots of aluminum. We have chosen the (100) plane in order to show both first and second layer atoms. Comparing with Fig. 1 of Ref. 15, we see much the same distribution of charge. In each figure the 3.4 contour is deflected toward nearest-neighbor atoms. Also, rectangular contours of 3.0 electrons per unit cell may be found in the fourfold interstitial regions.

In our double-layer plot we see that this 3.0 contour has reduced symmetry near the embedding surface (displayed as the dashed line). This is due to the last boundary condition imposed on the electrostatic potential—that the surface potential match the potential of the underlying bulk along the interface with the substrate. In this case the bulk potential has a muffin-tin form; and since the interface lies entirely in the interstitial region, the electrostatic potential along it must be everywhere equal to the bulk muffin-tin constant. This means that there is no lowering of the electrostatic potential along lines connecting atoms in the lowest surface layer to their near neighbors in the bulk. Thus, the electronic charge density along such lines is reduced from that between near neighbors in the surface region. This gives the observed asymmetry in the 3.0 and other contours. We see, however, that the healing length for any such imperfection in the boundary condition is quite short. In fact, the charge density is still fairly accurate *across* the embedding surface since it is constructed from wave functions which match on to exact solutions in the bulk. The problem may be eliminated altogether by making use of a warped muffin-tin potential for the bulk which would give a range of values for the electrostatic potential along the embedding surface.

The total charge in the surface region of the two-layer calculation is $5.893e$, but the total change in charge from the generalized phase shift (see Ref. 10), is $5.982e$. This is very close to exact overall charge neutrality, and is achieved automatically in the self-consistency procedure.

D. Surface states

The surface density of states at $\bar{\Gamma}$ from our double layer is shown in Fig. 8. The energy has been shifted off the real axis by 0.001 a.u. so that the discrete surface states are broadened slightly and can be found with the same numerical techniques that we use in the continuum. The surface state is very prominent, and is located only 0.007 a.u. (0.18 eV) above the bottom of the bulk band gap between 0.204 to 0.243 a.u. in the figure. (The Fermi energy is at 0.3085 a.u. relative to the bulk muffin-tin zero.) Both the absolute position of this state, 2.65 eV below E_F, and, more significantly, its energy relative to the bottom of the band gap are in good agreement with experiment.[17] The band gap itself is much narrower than the experimental value (1.06 eV compared with 1.68 eV), with the upper band edge apparently 0.6 eV too low; this problem in the *bulk* electronic structure may be due to inadequacies in the local density model for exchange correlation.

The charge-density contours of our $\bar{\Gamma}$ surface state (Fig. 9) are very similar to those of Krakauer, Posternak, Freeman, and Koelling.[15] We observe a slightly greater charge density on the vacuum side of the topmost atomic layer. Between the atomic layers the charge density is rather flat, peaking at approximately 0.4 electrons per bulk unit cell. This is a Shockley state resulting from the change in the boundary condition on the wave functions at the surface. It decays only slowly into the bulk[18] with a decay length that is estimated to be 7 atomic layers.[10]

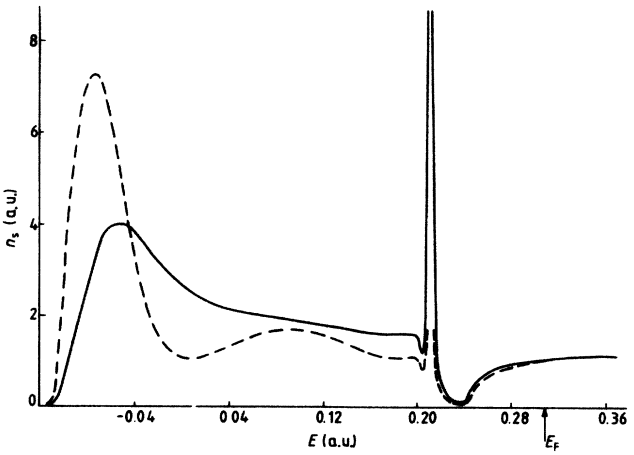

FIG. 8. The Al(001) surface density of states at $\bar{\Gamma}$. Full curve, top layer of atoms; dashed curve, second layer. Imaginary part of energy $=0.001$ a.u.

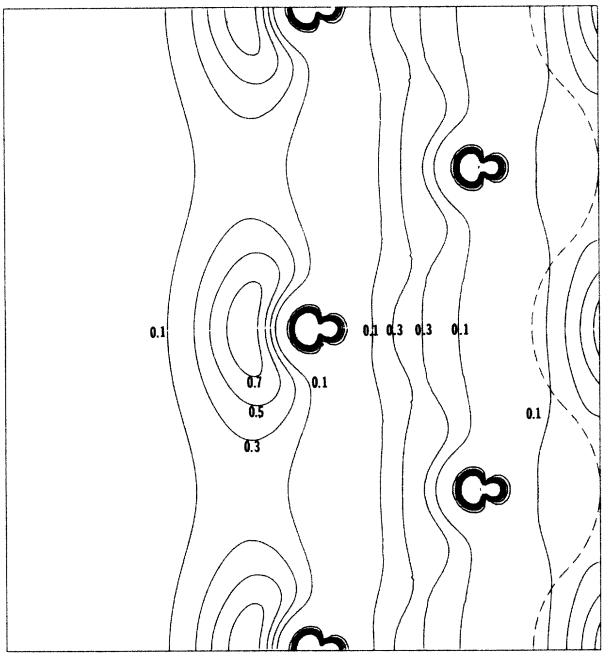

FIG. 9. The Al(001) $\bar{\Gamma}$ surface state charge density in units of electrons per bulk unit cell.

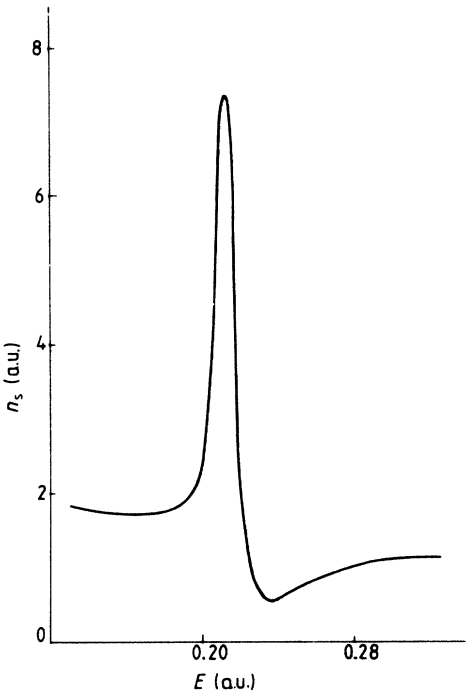

FIG. 10. The Al(001) surface density of states at $\bar{\Gamma}$ in the top layer of atoms. Imaginary part of energy = 0.005 a.u.

A pair of such states, arising from the two surfaces of a slab, interact even when the slab is fairly thick. They mix to form even and odd states split in energy by about 1 eV in the nine-layer slab calculations.

The $\bar{\Gamma}$ surface state is found to have an asymmetrical line shape in photoemission, smeared toward low energy:[17,19] this is probably due to the combined effects of broadening the surface state and the adjacent band edge. In the bulk the one-dimensional density of states (that is, at fixed wave vector parallel to the surface) has $E^{-1/2}$ singularities at band edges, which are suppressed at the surface. However, we see from Fig. 8 that the surface density of states is fairly constant up to the lower band edge where it drops off abruptly. When this feature is broadened together with the surface state by working with an imaginary energy of 0.005 a.u., an apparently asymmetric surface peak is produced (Fig. 10), having the line shape seen experimentally.[19] The experimental broadening could be due to either hole lifetime or instrumental effects. The apparent merging of the surface state with the lower band edge is also the reason for the band edge not being seen in photoemission experiments from Mg(0001). At the upper band edge, the surface density of states is completely rounded off, with no sign of the bulk $E^{-1/2}$ singularity even on the second layer of atoms. This suppression of the density of states at the upper band edge would give an apparent increase in the band gap in surface photoemission. However, its effect on direct transition measurements is not obvious, and it is not clear if this contributes to the increased band gap measured experimentally compared with band-structure calculations.

Moving out to $\bar{X}$ in the surface Brillouin zone, a surface state is measured experimentally at 4.55 eV below E_F, associated with the gap at L in the bulk band structure.[19] Our calculation gives the surface state at 0.139 a.u. relative to the zero of energy, with band edges at 0.136 a.u. and 0.148 a.u.; the non-self-consistent calculation of Spanjaard, Jepsen, and Marcus[20] also puts the state very close to the bottom of this narrow gap. The energy of our state is 4.61 eV below the Fermi energy, in excellent agreement with experiment.

E. Resonance behavior

For $\mathbf{K}$ near $\bar{\Gamma}$ the bulk aluminum band gap remains absolute; however, as one moves out toward the boundary of the surface zone, other bands cause the gap to narrow and then close. Photoemission studies show that a sharp surface peak persists even after the gap closes.[21] The gap closes about midway between $\bar{\Gamma}$ and $\bar{M}$; but the band effecting the closure is one of *odd* symmetry with respect to reflection in the $\bar{\Gamma}\bar{M}$ line. Since the surface state is of *even* symmetry it cannot couple to the opposite symmetry bulk states, and thus remains a true surface state. This situation persists beyond $\mathbf{K}=(0.28,0.28)$, at which wave vector the surface state is pushed above E_F.

A much different situation occurs along $\bar{\Gamma}\bar{X}$. The gap is closed by an *even* symmetry (with respect to reflection now in the $\bar{\Gamma}\bar{X}$ line) bulk band at about $\mathbf{K}=(0.26,0)$. Beyond this wave vector, the *even* surface state may couple with *even* bulk bands and thus becomes a surface resonance. Electronic charge is no longer confined to the surface and may leak out into the bulk. Experiment, however, shows that the peak remains sharp.[21]

In Figs. 11 and 12 we display the calculated surface

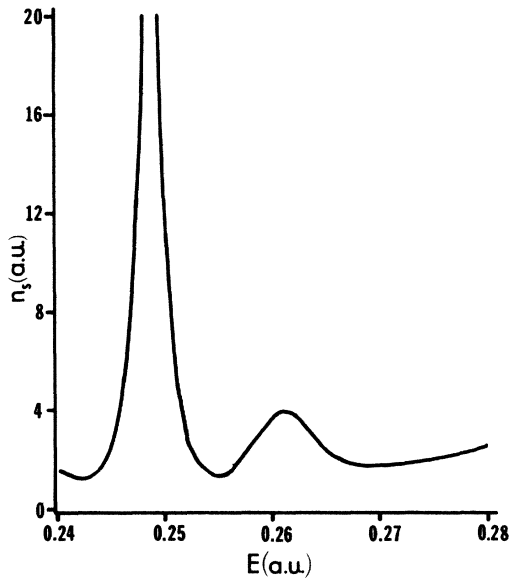

FIG. 11. The surface density of states at $\mathbf{K}=(0.25,0)$ in the top layer of atoms. Imaginary part of energy $=0.001$ a.u.

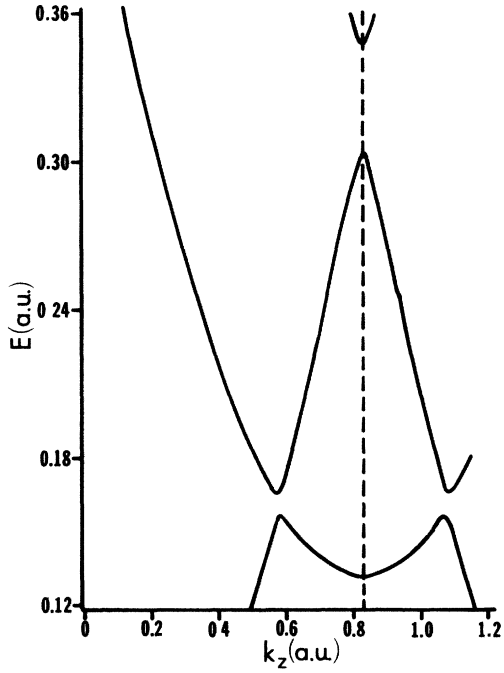

FIG. 13. Projected Al bulk band structure corresponding to $\mathbf{K}=(0.40,0)$.

density of states (DOS) for the surface state at $\mathbf{K}=(0.25,0)$ and the surface resonance at $\mathbf{K}=(0.40,0)$. Although broadened slightly by hybridization, the (0.40,0) resonance remains very sharp. This occurs because the coupling is mediated through the (weak) V_{111} component of the pseudopotential. This may be seen in the bulk band structure corresponding to $\mathbf{K}=(0.40,0)$, Fig. 13. The large gap extending from 0.30 to 0.35 hartrees is mediated by the V_{020} component of the pseudopotential (i.e., $\Delta E=2\,|\,V_{020}\,|\,$). Similarly, the small gap extending from 0.155 to 0.165 a.u. is mediated by the V_{111} component. Thus the bandstructure itself indicates that the V_{111} component is only a fraction as large as the V_{020} component. The relative weakness of V_{111} is confirmed by experiment: $|\,V_{111}\,|=0.0089$ a.u. vs $|\,V_{020}\,|=0.0281$ a.u.[22]

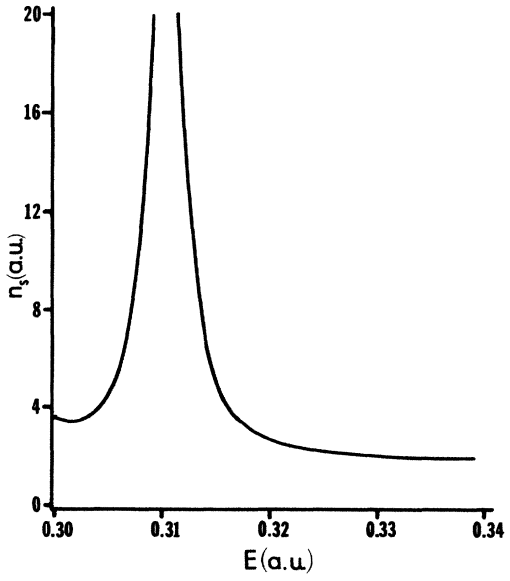

FIG. 12. The surface density of states at $\mathbf{K}=(0.40,0)$ in the top layer of atoms. Imaginary part of energy $=0.001$ a.u.

Once the gap closes along $\bar{\Gamma}\bar{X}$ the surface resonance continues to reside in the (020) partial band gap, coupling only weakly to the bulk bands through V_{111}. We also see additional surface structure in the small (111) hybridization gap, corresponding to the secondary peak seen at higher binding by Hansson and Flodström.[21] However, the weight in this secondary peak remains small, again corresponding to the relative sizes of V_{111} and V_{020}.

V. Ni(001) RESULTS

A. Charge density and work function

We have carried out a self-consistent calculation of the electronic structure of Ni(001) using a single layer embedded onto the substrate. The embedding potential is calculated from a Ni muffin-tin potential taken from the central layer of an earlier slab calculation. With a layer thickness $D=4.7$ a.u. and the distance defining plane waves $\tilde{D}=6$ a.u., we find that 80 LAPW's provide sufficient accuracy. The resulting charge density is shown in Fig. 14, corresponding to a work function of 5.71 eV, compared with the experimental value of 5.22 eV. There is obviously room for improvement here, particularly in the choice of embedding potential. Our bulk band structure (Fig. 15), for example, is somewhat

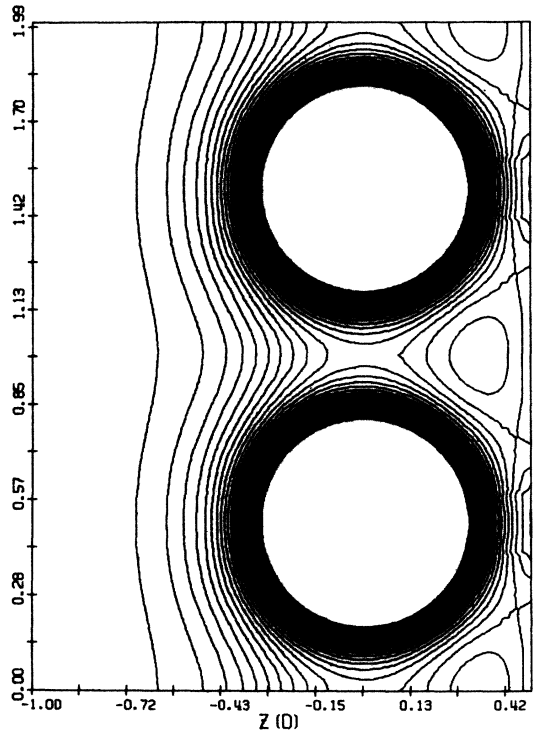

FIG. 14. Self-consistent total valence charge density in the (110) bulk Ni plane: 80 LAPW's, $\tilde{D}=6$ a.u. Lowest contour has $\rho=0.004$ a.u.; successive contours differ by 0.004 a.u.

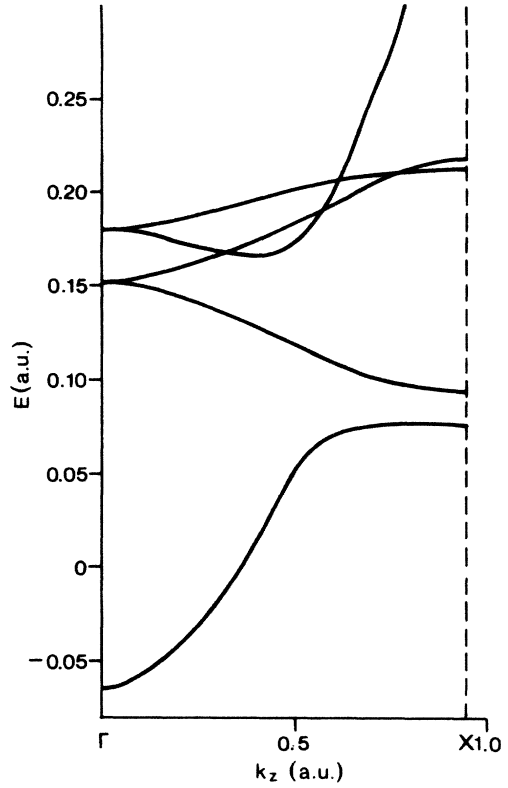

FIG. 15. Ni band structure in ⟨001⟩ direction along ΓX from the Moruzzi, Janak, and Williams (Ref. 23) potential.

different from that of Moruzzi, Janak, and Williams[23]—having a bandwidth of occupied states of 0.28 a.u. compared with their value of 0.33 a.u. Another source of difficulty in the calculation is the bulk potential at the interface with the substrate (Sec. III B), taken as the plane halfway between atomic layers with the caps of the muffin tins on either side (Fig. 2). To check the effect of the electrostatic boundary condition, we have shifted this potential by −0.075 a.u., which reduces the work function to 5.65 eV. It is remarkable that a comparatively large shift in the potential boundary condition produces such a small shift in the work function—due, of course, to the excellent screening in the metal. Although our work function is too large, it is not out of line with the values of 5.5 and 5.37 eV found in (spin-polarized) five- and seven-layer slab calculations.[24,25]

B. Surface density of states

The surface density of states at $\mathbf{K}=\mathbf{0}$ is shown in Fig. 16. The lowest-lying feature, the peak at $E=0.08$ a.u. is a weak surface state right at the X_1 band edge at the top of the lowest Δ_1 band (Fig. 15). The feature above is associated with $\Delta_{2'}$ bulk states at the surface. The large feature at 0.166 a.u., 1.3 eV below the Fermi energy, lies just below the minimum of the upper Δ_1 band, and is a second surface state of Δ_1 symmetry consisting mainly of the d_{z^2} orbital. Experimentally, there seems no evidence of these two surface states,[26,27] but this may be due to lifetime broadening which is large in Ni: for the state at −1.3 eV this is likely to be of the order of 0.5 eV. However, a rather featureless peak is seen with a width quite close to that of the states shown in Fig. 16 between 0.16 a.u. and the Fermi energy.

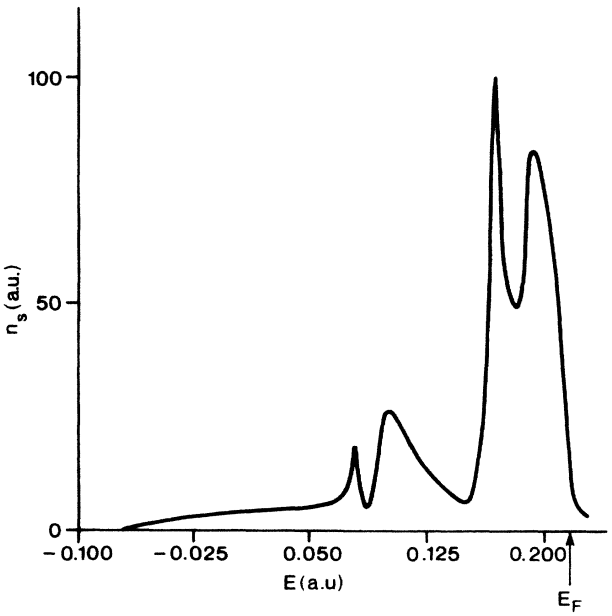

FIG. 16. The Ni(001) surface density of states at $\bar{\Gamma}$.

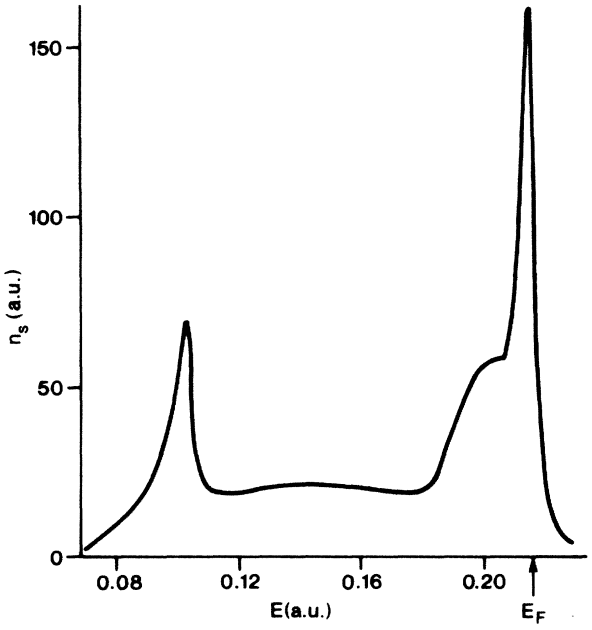

FIG. 17. The Ni(001) surface density of states at $\bar{M}$.

At $\bar{M}$, in the corner of the surface Brillouin zone, we obtain the surface density of states shown in Fig. 17. The most prominent feature is a Tamm surface state at 0.215 a.u., the Fermi energy. This is made up of d_{xy} orbitals, is highly localized on the surface atoms, and, in this calculation, lies 0.1 eV below the corresponding bulk band. In their seven-layer slab calculation,[25] Wimmer, Freeman, and Krakauer find the spin-split majority-spin Tamm state 0.14 eV below the Fermi energy, pushed above the corresponding bulk band by 0.24 eV. Experimentally, the Tamm state is seen 0.05 eV below the Fermi energy,[28] shifted only slightly upwards from the bulk majority-spin band which, in a band structure fitted to experiment,[29] lies 0.10 eV below E_F. Clearly our paramagnetic calculation positions the Tamm state too low in energy; it should lie just above the bulk band at about 0.220 a.u. This highlights perhaps the main problem in obtaining accurate densities of states in the SEGF approach—getting a good bulk potential which is completely compatible with the surface formalism, preferably using a similar basis and sampling **k**-space in an equivalent way in the self-consistency procedure. Nevertheless, our *single*-layer calculation, using a simple choice of bulk potential for the embedding, is able to give a reasonable description of the Ni(001) surface electronic structure.

VI. CONCLUSIONS

From this work we see that the SEGF method provides a simple way of calculating surface electronic structure. Its advantages are that it gives the electronic structure of a real semi-infinite system, treating the continuum of bulk states as well as the discrete surface states correctly, and that it concentrates on the surface region, requiring only relatively small basis sets. We are presently applying the method to other metal surfaces, with and without overlayers, and to semiconductors.

Remaining problems with the method are all associated with our present technique for calculating the embedding potential: using the layer-doubling method with the muffin-tin potential from a separate bulk calculation for the substrate. This means that the self-consistency in the bulk is not completely compatible with that in the surface—for example, the muffin-tin potential will vary somewhat with different wave vector sampling. Our simplified treatment of the substrate also restricts our knowledge of the potential on the interface between bulk and surface (used for solving Poisson's equation, see Sec. III B). To a large extent, both of these problems are minimized by the short screening length in metals; but difficulties remain, such as the shape of the Al(001) charge density at the interface with the substrate, and the poor work function in the single-layer Ni(001) calculation. The problems should be resolved when we finally adapt a bulk LAPW program to give the embedding potential on the same footing as the surface potential.

ACKNOWLEDGMENT

One of us (G.A.B.) gratefully acknowledges financial support of The Robert A. Welch Foundation (Houston, TX), under Grant No. AA-1033.

APPENDIX A: MATCHING CONDITIONS

As in the film LAPW formalism, the coefficients of the radial muffin-tin solutions in Eq. (16) are obtained by requiring that each basis function and its first derivative be continuous across the MT-sphere boundary for each angular-momentum component. Thus

$$A^{\pm}_{L,\alpha}=\frac{4\pi\rho_\alpha^2}{\sqrt{\Omega}}\exp(i\mathbf{K}_m\cdot\mathbf{R})a_{l,\alpha}(m,n)Y^{\pm}_{L,\alpha}(m,n)\ ,$$
$$B^{\pm}_{L,\alpha}=\frac{4\pi\rho_\alpha^2}{\sqrt{\Omega}}\exp(i\mathbf{K}_m\cdot\mathbf{R})b_{l,\alpha}(m,n)Y^{\pm}_{L,\alpha}(m,n)\ , \tag{A1}$$

where ρ_α is the radius of MT α, centered on $(\mathbf{R}_\alpha,z_\alpha)$,

$$a_{l,\alpha}(m,n)=\frac{\frac{\partial j_l(K_{mn}\rho_\alpha)}{\partial\rho}\dot{u}_{l,\alpha}(\rho_\alpha)-j_l(K_{mn}\rho_\alpha)\frac{\partial\dot{u}_{l,\alpha}(\rho_\alpha)}{\partial\rho}}{\rho_\alpha^2\left[\dot{u}_{l,\alpha}(\rho_\alpha)\frac{\partial u_{l,\alpha}(\rho_\alpha)}{\partial\rho}-u_{l,\alpha}(\rho_\alpha)\frac{\partial\dot{u}_{l,\alpha}(\rho_\alpha)}{\partial\rho}\right]}\ ,$$

$$b_{l,\alpha}(m,n)=\frac{j_1(K_{mn}\rho_\alpha)\dfrac{\partial u_{l,\alpha}(\rho_\alpha)}{\partial\rho}-\dfrac{\partial j_1(K_{mn}\rho_\alpha)}{\partial\rho}u_{l,\alpha}(\rho_\alpha)}{\rho_\alpha^2\left[\dot{u}_{l,\alpha}(\rho_\alpha)\dfrac{\partial u_{l,\alpha}(\rho_\alpha)}{\partial\rho}-u_{l,\alpha}(\rho_\alpha)\dfrac{\partial\dot{u}_{l,\alpha}(\rho_\alpha)}{\partial\rho}\right]},$$

$$Y^{\pm}_{L,\alpha}(m,n)=\frac{1}{\sqrt{2}}[\exp(ik_nz_\alpha)Y^*_L(\hat{\mathbf{K}}^{+}_{mn})\pm\exp(-ik_nz_\alpha)Y^*_L(\hat{\mathbf{K}}^{-}_{mn})],$$

$$\mathbf{K}^{+}_{mn}=\mathbf{K}_m+k_n\hat{\mathbf{z}},\ \text{and}\ \mathbf{K}^{-}_{mn}=\mathbf{K}_m-k_n\hat{\mathbf{z}}\ .$$

In these formulas the upper sign refers to the even (cosine) LAPW's, and the lower sign refers to the odd (sine) LAPW's. $u_{l,\alpha}$ and $\dot{u}_{l,\alpha}$ are the solutions of the radial scalar-relativistic wave equation in the MT spheres.

The vacuum coefficients, Eq. (17), are given by

$$\alpha^{\pm}(m,n)=\frac{1}{\sqrt{2\Omega}}\left[\frac{\partial v_m}{\partial z}(-D/2)\times\begin{Bmatrix}\cos(k_nD/2)\\-\sin(k_nD/2)\end{Bmatrix}-v_m(-D/2)k_n\times\begin{Bmatrix}\sin(k_nD/2)\\\cos(k_nD/2)\end{Bmatrix}\right],$$

$$\beta^{\pm}(m,n)=\frac{1}{\sqrt{2\Omega}}\left[\frac{\partial v_m}{\partial z}(-D/2)\times\begin{Bmatrix}-\cos(k_nD/2)\\\sin(k_nD/2)\end{Bmatrix}-v_m(-D/2)k_n\times\begin{Bmatrix}\sin(k_nD/2)\\\cos(k_nD/2)\end{Bmatrix}\right], \tag{A2}$$

where again the upper function refers to even and the lower to odd LAPW's. $v_m(z)$ and $\dot{v}_m(z)$ are the solutions of the vacuum Schrödinger equation. The geometry is that shown in Fig. 2, with positive z directed into the solid.

APPENDIX B: OVERLAP IN THE INTERSTITIAL REGION

The contribution to the overlap integral from the interstitial region is

$$O_{m'n';mn}=\frac{2}{\Omega}\left[\int_{-D/2}^{\zeta}dz\int_{\text{2D cell}}d^2\mathbf{R}\exp[i(\mathbf{G}_m-\mathbf{G}_{m'})\cdot\mathbf{R}]\times\begin{Bmatrix}\cos(k_{n'}z)\\\sin(k_{n'}z)\end{Bmatrix}\times\begin{Bmatrix}\cos(k_nz)\\\sin(k_nz)\end{Bmatrix}\right.$$
$$\left.-\sum_{\text{MT's }\alpha}\int_{\mathbf{r}\in\alpha}d^3\mathbf{r}\exp[i(\mathbf{G}_m-\mathbf{G}_{m'})\cdot\mathbf{R}]\times\begin{Bmatrix}\cos(k_{n'}z)\\\sin(k_{n'}z)\end{Bmatrix}\times\begin{Bmatrix}\cos(k_nz)\\\sin(k_nz)\end{Bmatrix}\right]. \tag{B1}$$

In the even-even and odd-odd cases this becomes (upper and lower sign, respectively)

$$O_{m'n';mn}=\frac{\delta_{mm'}}{D}\left[\frac{\sin[(k_{n'}-k_n)D/2]}{k_{n'}-k_n}\pm\frac{\sin[(k_{n'}+k_n)D/2]}{k_{n'}+k_n}+\frac{\sin[(k_{n'}-k_n)\zeta]}{k_{n'}-k_n}\pm\frac{\sin[(k_{n'}+k_n)\zeta]}{k_{n'}+k_n}\right]$$
$$-\frac{4\pi}{\Omega}\sum_\alpha\rho_\alpha^2\exp[i(\mathbf{G}_m-\mathbf{G}_{m'})\cdot\mathbf{R}_\alpha]\{\cos[(k_{n'}-k_n)z_\alpha]J_\alpha(\mathbf{K}^{+}_{m'n'},\mathbf{K}^{+}_{mn})\pm\cos[(k_{n'}+k_n)z_\alpha]J_\alpha(\mathbf{K}^{+}_{m'n'},\mathbf{K}^{-}_{mn})\}\ , \tag{B2}$$

where

$$J_\alpha(\mathbf{K}_1,\mathbf{K}_2)=\frac{j_1(|\mathbf{K}_1-\mathbf{K}_2|\rho_\alpha)}{|\mathbf{K}_1-\mathbf{K}_2|}\ .$$

In the even-odd case the overlap is given by

$$O_{m'n';mn}=\frac{\delta_{mm'}}{D}\left[\frac{-\cos[(k_{n'}-k_n)D/2]}{k_{n'}-k_n}+\frac{\cos[(k_{n'}+k_n)D/2]}{k_{n'}+k_n}+\frac{\cos[(k_{n'}-k_n)\zeta]}{k_{n'}-k_n}-\frac{\cos[(k_{n'}+k_n)\zeta]}{k_{n'}+k_n}\right]$$
$$-\frac{4\pi}{\Omega}\sum_\alpha\rho_\alpha^2\exp[i(\mathbf{G}_m-\mathbf{G}_{m'})\cdot\mathbf{R}_\alpha]\{-\sin[(k_{n'}-k_n)z_\alpha]J_\alpha(\mathbf{K}^{+}_{m'n'},\mathbf{K}^{+}_{mn})+\sin[(k_{n'}+k_n)z_\alpha]J_\alpha(\mathbf{K}^{+}_{m'n'},\mathbf{K}^{-}_{mn})\}\ . \tag{B3}$$

APPENDIX C: HAMILTONIAN IN THE INTERSTITIAL REGION

The kinetic-energy contribution to the Hamiltonian is obviously

$$H^{\text{kin}}_{m'n';mn}=\frac{K_m^2+k_n^2}{2}O_{m'n';mn}\ . \tag{C1}$$

The matrix elements of the potential given by Eq. (18) are evaluated *not* over the integration region in Appendix B—that is, between $-D/2$ and ζ with the surface muffin-tin spheres entirely subtracted, but over the shaded region shown in Fig. 2. To obtain the shaded region, partial surface *and* substrate muffin-tins must be subtracted from the region between $-D/2$ and ζ. This corresponds to taking zero potential between the "true" embedding surface and the plane to which the embedding potential is transferred (Sec. II B). The matrix elements are then

$$H^{\text{pot}}_{m'n';mn}=\frac{2}{\Omega}\left[\int_{-D/2}^{\zeta}dz\int_{\text{2D cell}}d^2\mathbf{R}\exp[i(\mathbf{G}_m-\mathbf{G}_{m'})\cdot\mathbf{R}]\times\begin{Bmatrix}\cos(k_{n'}z)\\ \sin(k_{n'}z)\end{Bmatrix}\times\begin{Bmatrix}\cos(k_nz)\\ \sin(k_nz)\end{Bmatrix}\times V(\mathbf{r})\right.$$
$$-\sum_{\text{MT's }\alpha}\int_{\mathbf{r}\in\alpha}d^3\mathbf{r}\exp[i(\mathbf{G}_m-\mathbf{G}_{m'})\cdot\mathbf{R}]\times\begin{Bmatrix}\cos(k_{n'}z)\\ \sin(k_{n'}z)\end{Bmatrix}\times\begin{Bmatrix}\cos(k_nz)\\ \sin(k_nz)\end{Bmatrix}\times V(\mathbf{r})$$
$$\left.\pm\sum_{\text{MT's }\beta}\int_{\mathbf{r}\in\text{ cap of }\beta}d^3\mathbf{r}\exp[i(\mathbf{G}_m-\mathbf{G}_{m'})\cdot\mathbf{R}]\times\begin{Bmatrix}\cos(k_{n'}z)\\ \sin(k_{n'}z)\end{Bmatrix}\times\begin{Bmatrix}\cos(k_nz)\\ \sin(k_nz)\end{Bmatrix}\times V(\mathbf{r})\right]. \tag{C2}$$

Muffin tins β are those in the surface region and substrate which cross the embedding plane; and the integrals are over the caps truncated by the plane $z=\zeta$. The $+$ sign is for surface MT spheres, correcting the previous integral which subtracted the entire sphere. The $-$ sign, for substrate muffin tins, makes the correction required by Fig. 2. These correction terms for β MT spheres must be evaluated numerically.

Apart from these β corrections, the contribution to (C2) from

$$V_{m''n''}\exp(i\mathbf{G}_{m''}\cdot\mathbf{R})\times\begin{Bmatrix}\cos(k_{n''}z)\\ \sin(k_{n''}z)\end{Bmatrix}$$

is then easily evaluated, as in (B2) and (B3):

$$H^{\text{pot}}_{m'n';mn}=\frac{V_{m''n''}}{2}\sum_{i=1}^{4}\begin{Bmatrix}a_i\\ b_i\end{Bmatrix}\times\left[\frac{\delta_{m'',m'-m}}{\kappa_iD}\times\begin{Bmatrix}[\sin(\kappa_i\zeta)+\sin(\kappa_iD/2)]\\ [-\cos(\kappa_i\zeta)+\cos(\kappa_iD/2)]\end{Bmatrix}\right.$$
$$-\frac{4\pi}{\Omega}\sum_{\alpha}\rho_\alpha^2\exp[i(\mathbf{G}_m+\mathbf{G}_{m''}-\mathbf{G}_{m'})\cdot\mathbf{R}_\alpha]\times\begin{Bmatrix}\cos(\kappa_iz_\alpha)\\ \sin(\kappa_iz_\alpha)\end{Bmatrix}$$
$$\left.\times\frac{j_1(|\mathbf{G}_m+\mathbf{G}_{m''}-G_{m'}+\kappa_i\hat{\mathbf{z}}|\rho_\alpha)}{|\mathbf{G}_m+\mathbf{G}_{m''}-\mathbf{G}_{m'}+\kappa_i\hat{\mathbf{z}}|}\right]. \tag{C3}$$

The coefficients a_i with the upper functions, and coefficients b_i with the lower functions, come from rewriting the trigonometric functions in the integrals as

$$\begin{Bmatrix}\cos(k_{n'}z)\\ \sin(k_{n'}z)\end{Bmatrix}\times\begin{Bmatrix}\cos(k_{n''}z)\\ \sin(k_{n''}z)\end{Bmatrix}\times\begin{Bmatrix}\cos(k_nz)\\ \sin(k_nz)\end{Bmatrix}=\tfrac{1}{4}\sum_{i=1}^{4}[a_i\cos(\kappa_iz)+b_i\sin(\kappa_iz)] \tag{C4}$$

with

$(a_1,a_2,a_3,a_4)=(1,1,1,1)$ and $(b_1,b_2,b_3,b_4)=(0,0,0,0)$ for $\cos(k_{n'}z)\cos(k_{n''}z)\cos(k_nz)$,

$(a_1,a_2,a_3,a_4)=(0,0,0,0)$ and $(b_1,b_2,b_3,b_4)=(-1,1,1,1)$ for $\cos(k_{n'}z)\cos(k_{n''}z)\sin(k_nz)$,

$(a_1,a_2,a_3,a_4)=(0,0,0,0)$ and $(b_1,b_2,b_3,b_4)=(1,-1,1,1)$ for $\cos(k_{n'}z)\sin(k_{n''}z)\cos(k_nz)$,

$(a_1,a_2,a_3,a_4)=(1,1,-1,-1)$ and $(b_1,b_2,b_3,b_4)=(0,0,0,0)$ for $\cos(k_{n'}z)\sin(k_{n''}z)\sin(k_nz)$,

$(a_1,a_2,a_3,a_4)=(1,-1,1,-1)$ and $(b_1,b_2,b_3,b_4)=(0,0,0,0)$ for $\sin(k_{n'}z)\cos(k_{n''}z)\sin(k_nz)$,

$(a_1,a_2,a_3,a_4)=(0,0,0,0)$ and $(b_1,b_2,b_3,b_4)=(1,1,1,-1)$ for $\sin(k_{n'}z)\sin(k_{n''}z)\sin(k_nz)$,

and

$$\kappa_1=(k_{n'}+k_{n''}-k_n),\quad \kappa_2=(k_{n'}-k_{n''}+k_n),\quad \kappa_3=(-k_{n'}+k_{n''}+k_n),\quad \kappa_4=(k_{n'}+k_{n''}+k_n).$$

Turning to the matrix element of the linear term V_1z, the first integral in (C2) between $-D/2$ and ζ is elementary. To evaluate the integrals over the muffin tins α, we expand the plane waves and z in spherical harmonics, giving

$$H^{\rm pot}_{m'n';mn}=V_1\sum_{i=1}^{2}\begin{Bmatrix}a_i\\b_i\end{Bmatrix}\times\left[\frac{\delta_{m',m}}{\kappa_i^2 D}\begin{Bmatrix}[\cos(\kappa_i\zeta)-\cos(\kappa_i D/2)+\kappa_i\zeta\sin(\kappa_i\zeta)-\kappa_i\sin(\kappa_i D/2)D/2]\\[\sin(\kappa_i\zeta)+\sin(\kappa_i D/2)-\kappa_i\zeta\cos(\kappa_i\zeta)-\kappa_i\cos(\kappa_i D/2)D/2]\end{Bmatrix}\right.$$
$$-\frac{4\pi}{\Omega}\sum_\alpha\rho_\alpha^3\exp[i(\mathbf{G}_m-\mathbf{G}_{m'})\cdot\mathbf{R}_\alpha]\left[\begin{Bmatrix}\cos(\kappa_i z_\alpha)\\\sin(\kappa_i z_\alpha)\end{Bmatrix}\times\frac{z_\alpha j_1(|\mathbf{G}_m-\mathbf{G}_{m'}+\kappa_i\hat{\mathbf{z}}|\rho_\alpha)}{|\mathbf{G}_m-\mathbf{G}_{m'}+\kappa_i\hat{\mathbf{z}}|\rho_\alpha}\right.$$
$$+\begin{Bmatrix}-\sin(\kappa_i z_\alpha)\\\cos(\kappa_i z_\alpha)\end{Bmatrix}$$
$$\left.\left.\times\frac{\kappa_i j_2(|\mathbf{G}_m-\mathbf{G}_{m'}+\kappa_i\hat{\mathbf{z}}|\rho_\alpha)}{|\mathbf{G}_m-\mathbf{G}_{m'}+\kappa_i\hat{\mathbf{z}}|^2}\right]\right]. \tag{C5}$$

As above, the coefficients a_i and b_i come from the expansion

$$\begin{Bmatrix}\cos(k_{n'}z)\\\sin(k_{n'}z)\end{Bmatrix}\times\begin{Bmatrix}\cos(k_n z)\\\sin(k_n z)\end{Bmatrix}=\tfrac{1}{2}\sum_{i=1}^{2}[a_i\cos(\kappa_i z)+b_i\sin(\kappa_i z)] \tag{C6}$$

with

$(a_1,a_2)=(1,1)$ and $(b_1,b_2)=(0,0)$ for $\cos(k_{n'}z)\cos(k_n z)$,

$(a_1,a_2)=(0,0)$ and $(b_1,b_2)=(-1,1)$ for $\cos(k_{n'}z)\sin(k_n z)$,

$(a_1,a_2)=(1,-1)$ and $(b_1,b_2)=(0,0)$ for $\sin(k_{n'}z)\sin(k_n z)$,

and $\kappa_1=(k_{n'}-k_n)$ and $\kappa_2=(k_{n'}+k_n)$.

The matrix elements of the quadratic term are a little more complicated but can be found in an analogous way. Most difficult are the matrix elements of the exponential terms in Eq. (18):

$$V_{m''}\pm\exp(\pm G_{m''}z)\exp(i\mathbf{G}_{m''}\cdot\mathbf{R}).$$

Again the integral between $-D/2$ and ζ is easy, but in the MT spheres we need the integral of

$$\exp[i(\mathbf{G}_m+\mathbf{G}_{m''}-G_{m'})\cdot\mathbf{R}_\alpha]\exp(G_{m''}z)\exp(i\kappa_i z).$$

This is a plane wave with complex energy and wave vector, which can be expanded in spherical waves with complex argument. Upon integrating over the sphere, the only nonvanishing contribution comes from the first term in the expansion, $j_0(\kappa r)$, where $\kappa=(x,y)$, and

$$x=\frac{1}{\sqrt{2}}\{|\mathbf{G}_m+\mathbf{G}_{m''}-\mathbf{G}_{m'}|^2+\kappa_i^2-G_{m''}^2+[(|\mathbf{G}_m+\mathbf{G}_{m''}-\mathbf{G}_{m'}|^2+\kappa_i^2-G_{m''}^2)^2+4\kappa_i^2G_{m''}^2]^{1/2}\}^{1/2},$$
$$y=\pm\frac{1}{\sqrt{2}}\{-|\mathbf{G}_m+\mathbf{G}_{m''}-\mathbf{G}_{m'}|^2-\kappa_i^2+G_{m''}^2+[(|\mathbf{G}_m+\mathbf{G}_{m''}-\mathbf{G}_{m'}|^2+\kappa_i^2-G_{m''}^2)^2+4\kappa_i^2G_{m''}^2]^{1/2}\}^{1/2}, \tag{C7}$$

It then follows that

$$\int_0^{\rho_\alpha}d^3\mathbf{r}\exp[i(\mathbf{G}_m+\mathbf{G}_{m''}-\mathbf{G}_{m'})\cdot\mathbf{R}_\alpha]\exp(G_{m''}z)\exp(i\kappa_i z)=4\pi\rho_\alpha^2\frac{j_1((x+iy)\rho_\alpha)}{x+iy}. \tag{C8}$$

We then find that the contribution to the matrix element from $V_{m+}\exp(G_{m''}z)\exp(i\mathbf{G}_{m''}\cdot\mathbf{R})$ is

$$H^{\rm pot}_{m'n';mn}=V_{m''}+\sum_{i=1}^{2}a_i\left[\frac{\delta_{m'',m'-m}}{D(G_{m''}^2+\kappa_i^2)}[G_{m''}\cos(\kappa_i\zeta)\exp(G_{m''}\zeta)+\kappa_i\sin(\kappa_i\zeta)\exp(G_{m''}\zeta)\right.$$
$$\left.-G_{m''}\cos(\kappa_i D/2)\exp(-G_{m''}D/2)+\kappa_i\sin(\kappa_i D/2)\exp(-G_{m''}D/2)]\right.$$
$$\left.-\frac{4\pi}{\Omega}\sum_\alpha\rho_\alpha^2\exp[i(\mathbf{G}_m+\mathbf{G}_{m''}-\mathbf{G}_{m'})\cdot\mathbf{R}_\alpha]\exp(G_{m''}z_\alpha)\mathrm{Re}\left[\exp(i\kappa_i z_\alpha)\frac{j_1((x+iy)\rho_\alpha)}{x+iy}\right]\right] \tag{C9}$$

or

$$H^{\rm pot}_{m'n';mn}=V_{m''}+\sum_{i=1}^{2}b_i\left[\frac{\delta_{m'',m'-m}}{D(G^2_{m''}+\kappa_i^2)}[G_{m''}\sin(\kappa_i\zeta)\exp(G_{m''}\zeta)-\kappa_i\cos(\kappa_i\zeta)\exp(G_{m''}\zeta)\right.$$

$$+G_{m''}\sin(\kappa_i D/2)\exp(-G_{m''}D/2)+\kappa_i\cos(\kappa_i D/2)\exp(-G_{m''}D/2)]$$

$$\left.-\frac{4\pi}{\Omega}\sum_{\alpha}\rho_\alpha^2\exp[i(\mathbf{G}_m+\mathbf{G}_{m''}-\mathbf{G}_{m'})\cdot\mathbf{R}_\alpha]\exp(G_{m''}z_\alpha)\mathrm{Im}\left[\exp(i\kappa_i z_\alpha)\frac{j_1((x+iy)\rho_\alpha)}{x+iy}\right]\right].$$

There is a similar expression for the contribution from $V_{m\_}\exp(-G_{m''}z)\exp(i\mathbf{G}_{m''}\cdot\mathbf{R})$.

APPENDIX D: OVERLAP IN THE MT SPHERES

The overlap contribution from muffin tin α can be written in terms of coefficients $A^{\pm}_{L,\alpha}$ and $B^{\pm}_{L,\alpha}$ as

$$O^{(\alpha)}_{m'n';mn}=\sum_L[A^{\pm *}_{L,\alpha}(m',n')A^{\pm}_{L,\alpha}(m,n)+B^{\pm *}_{L,\alpha}(m',n')B^{\pm}_{L,\alpha}(m,n)N_{l,\alpha}]\ , \tag{D1}$$

where $N_{l,\alpha}$ is the normalization of $\dot{u}_{l,\alpha}(r)$ through the muffin-tin sphere. ($u_{l,\alpha}$ and $\dot{u}_{l,\alpha}$ are orthogonal.) In the even-even and odd-odd cases, Eq. (D1) can be rewritten as

$$O^{(\alpha)}_{m'n';mn}=\frac{4\pi}{\Omega}\rho_\alpha^4\exp[i(\mathbf{G}_m-\mathbf{G}_{m'})\cdot\mathbf{R}_\alpha]\sum_l(2l+1)[a_{l,\alpha}(m',n')a_{l,\alpha}(m,n)+b_{l,\alpha}(m',n')b_{l,\alpha}(m,n)N_{l,\alpha}]$$

$$\times\{\cos[(k_n-k_{n'})z_\alpha]P_l(\hat{\mathbf{K}}^{+}_{mn}\cdot\hat{\mathbf{K}}^{+}_{m'n'})\pm\cos[(k_n+k_{n'})z_\alpha]P_l(\hat{\mathbf{K}}^{+}_{mn}\cdot\hat{\mathbf{K}}^{-}_{m'n'})\}\ , \tag{D2}$$

where $a_{l,\alpha}$ and $b_{l,\alpha}$ are given in Appendix A, and the arguments of the Legendre polynomials are the cosines of the angles between $\mathbf{K}^{+}_{mn}$ and $\mathbf{K}^{\pm}_{m'n'}$.

Similarly, in the even-odd case the overlap is

$$O^{(\alpha)}_{m'n';mn}=\frac{4\pi}{\Omega}\rho_\alpha^4\exp[i(\mathbf{G}_m-\mathbf{G}_{m'})\cdot\mathbf{R}_\alpha]\sum_l(2l+1)[a_{l,\alpha}(m',n')a_{l,\alpha}(m,n)+b_{l,\alpha}(m',n')b_{l,\alpha}(m,n)N_{l,\alpha}]$$

$$\times\{\sin[(k_n-k_{n'})z_\alpha]P_l(\hat{\mathbf{K}}^{+}_{mn}\cdot\hat{\mathbf{K}}^{+}_{m'n'})+\sin[(k_n+k_{n'})z_\alpha]P_l(\hat{\mathbf{K}}^{+}_{mn}\cdot\hat{\mathbf{K}}^{-}_{m'n'})\}\ , \tag{D3}$$

APPENDIX E: HAMILTONIAN IN THE MT SPHERES

The matrix element of the nonspherical components of the potential, Eq. (19), must be found numerically. However, the contribution from the spherical part of the Hamiltonian can be found seminumerically, because $u_{l,\alpha}$ and $\dot{u}_{l,\alpha}$ are solutions of the scalar-relativistic equation with potential $V_0(r)$. Analogous to Eq. (D2) we have in the even-even and odd-odd cases:

$$H^{(\alpha)}_{m'n';mn}=\frac{4\pi}{\Omega}\rho_\alpha^4\exp[i\mathbf{G}_m-\mathbf{G}_{m'})\cdot\mathbf{R}_\alpha]\sum_l(2l+1)[a_{l,\alpha}(m',n')a_{l,\alpha}(m,n)E_{l,\alpha}$$

$$+b_{l,\alpha}(m',n')b_{l,\alpha}(m,n)\langle\dot{u}_{l,\alpha}\,|\,H\,|\,\dot{u}_{l,\alpha}\rangle$$

$$+a_{l,\alpha}(m',n')b_{l,\alpha}(m,n)\langle u_{l,\alpha}\,|\,H\,|\,\dot{u}_{l,\alpha}\rangle$$

$$+b_{l,\alpha}(m',n')a_{l,\alpha}(m,n)\langle\dot{u}_{l,\alpha}\,|\,H\,|\,u_{l,\alpha}\rangle]$$

$$\times\{\cos[(k_n-k_{n'})z_\alpha]P_l(\hat{\mathbf{K}}^{+}_{mn}\cdot\hat{\mathbf{K}}^{+}_{m'n'})\pm\cos[(k_n+k_{n'})z_\alpha]P_l(\hat{\mathbf{K}}^{+}_{mn}\cdot\hat{\mathbf{K}}^{-}_{m'n'})\}\ .$$

Because $u_{l,\alpha}$ satisfies $Hu_{l,\alpha}=E_{l,\alpha}u_{l,\alpha}$, and since $u_{l,\alpha}$ is orthogonal to $\dot{u}_{l,\alpha}$, we see that $\langle\dot{u}_{l,\alpha}\,|\,H\,|\,u_{l,\alpha}\rangle=0$. From the scalar-relativistic equation we can show that

$$\langle u_{l,\alpha} \mid H \mid \dot{u}_{l,\alpha} \rangle = 1 + \frac{E_{l,\alpha} - \langle u_{l,\alpha} \mid V_0 \mid u_{l,\alpha} \rangle}{2mc^2} \quad \text{and} \quad \langle \dot{u}_{l,\alpha} \mid H \mid \dot{u}_{l,\alpha} \rangle = E_{l,\alpha} N_{l,\alpha} - \frac{\langle \dot{u}_{l,\alpha} \mid V_0 \mid u_{l,\alpha} \rangle}{2mc^2} , \tag{E2}$$

where we have included the relativistic correction.

In the even-odd case the contribution is

$$H^{(\alpha)}_{m'n';mn} = \frac{4\pi}{\Omega} \rho_\alpha^4 \exp[i(\mathbf{G}_m - \mathbf{G}_{m'}) \cdot \mathbf{R}_\alpha] \sum_l (2l+1)[a_{l,\alpha}(m',n') a_{l,\alpha}(m,n) E_{l,\alpha} + b_{l,\alpha}(m',n') b_{l,\alpha}(m,n) \langle \dot{u}_{l,\alpha} \mid H \mid \dot{u}_{l,\alpha} \rangle$$
$$+ a_{l,\alpha}(m',n') b_{l,\alpha}(m,n) \langle u_{l,\alpha} \mid H \mid \dot{u}_{l,\alpha} \rangle]$$
$$\times \{ \sin[(k_n - k_{n'}) z_\alpha] P_l(\hat{\mathbf{K}}^+_{mn} \cdot \hat{\mathbf{K}}^+_{m'n'}) + \sin[(k_n + k_{n'}) z_\alpha] P_l(\hat{\mathbf{K}}^+_{mn} \cdot \hat{\mathbf{K}}^-_{m'n'}) \} .$$

APPENDIX F: OVERLAP IN THE VACUUM REGION

The overlap contribution in the vacuum region is given by

$$O_{m'n';mn} = A \delta_{mm'} [\alpha^\pm(m,n') \alpha^\pm(m,n) + \beta^\pm(m,n') \beta^\pm(m,n) N_m] , \tag{F1}$$

where $\alpha^\pm$ and $\beta^\pm$ are as given in Appendix A. N_m is the normalization of $\dot{v}_m(z)$ through the vacuum region and A is the area of the 2D unit cell.

APPENDIX G: HAMILTONIAN IN THE VACUUM REGION

The matrix element of the planar-averaged part of the Hamiltonian is given by

$$H_{m'n';mn} = A \delta_{mm'} \{ E_v [a^\pm(m,n') \alpha^\pm(m,n) + \beta^\pm(m,n') \beta^\pm(m,n) N_m] + \alpha^\pm(m,n') \beta^\pm(m,n) \} , \tag{G1}$$

where E_v is the energy at which $v_m(z)$ satisfies the Schrödinger equation with potential $V_0(z)$, Eq. (20). The matrix elements of the higher Fourier components of the potential are found numerically.

APPENDIX H: EMBEDDING CONTRIBUTION TO THE HAMILTONIAN

The matrix element of the embedding potential is given by Eq. (21); however, we must also add the derivative contribution to the Hamiltonian, Eq. (7):

$$\tfrac{1}{2} \int_S d^2\mathbf{r}_S \chi^*_{m'n'} \frac{\partial \chi_{mn}}{\partial n_S} = \delta_{mm'} \frac{k_n}{D} \times \begin{Bmatrix} \cos(k_n \xi) \\ \sin(k_n \xi) \end{Bmatrix} \times \begin{Bmatrix} -\sin(k_n \xi) \\ \cos(k_n \xi) \end{Bmatrix} . \tag{H1}$$

This term ensures the overall hermiticity of $H_{m'n';mn}$.

[1] N. D. Lang and W. Kohn, Phys. Rev. B **3**, 1215 (1971).
[2] J. A. Appelbaum and D. R. Hamann, Phys. Rev. B **6**, 2166 (1972).
[3] H. Krakauer, M. Posternak, and A. J. Freeman, Phys. Rev. Lett. **41**, 1072 (1979).
[4] J. E. Inglesfield, J. Phys. C **14**, 3795 (1981).
[5] G. A. Benesh and J. E. Inglesfield, J. Phys. C **17**, 1595 (1984).
[6] G. A. Benesh and J. E. Inglesfield, J. Phys. C **19**, L539 (1986).
[7] J. B. Pendry, *Low Energy Electron Diffraction* (Academic, London, 1974).
[8] H. Krakauer, M. Posternak, and A. J. Freeman, Phys. Rev. B **19**, 1706 (1979).
[9] S. L. Cunningham, Phys. Rev. B **10**, 4988 (1974).
[10] J. E. Inglesfield and G. A. Benesh, Surf. Sci. (to be published).
[11] M. Weinert, J. Math. Phys. **22**, 2433 (1981).
[12] J. K. Grepstad, P. O. Gartland, and B. J. Slagsvold, Surf. Sci. **57**, 348 (1976).
[13] R. M. Eastment and C. H. B. Mee, J. Phys. F **3**, 1738 (1973).
[14] G. A. Benesh, H. Krakauer, D. E. Ellis, and M. Posternak, Surf. Sci. **104**, 599 (1981).
[15] H. Krakauer, M. Posternak, A. J. Freeman, and D. D. Koelling, Phys. Rev. B **23**, 3859 (1981).
[16] E. Wimmer, M. Weinert, A. J. Freeman, and H. Krakauer, Phys. Rev. B **24**, 2292 (1981).
[17] E. W. Plummer, Surf. Sci. **152/153**, 162 (1985).
[18] J. E. Inglesfield, Rep. Prog. Phys. **45**, 223 (1982).
[19] H. J. Levinson, F. Greuter, and E. W. Plummer, Phys. Rev. B **27**, 727 (1983).
[20] D. Spanjaard, D. W. Jepsen, and P. M. Marcus, Phys. Rev. B **19**, 642 (1979).
[21] G. V. Hansson and S. A. Flodström, Phys. Rev. B **18**, 1562 (1978).
[22] M. L. Cohen and V. Heine, in *Solid State Physics*, edited by H. Ehrenreich, F. Seitz, and D. Turnbull (Academic, New York, 1970), Vol. 24, p. 37.
[23] V. L. Moruzzi, J. F. Janak, and A. R. Williams, *Calculated Electronic Properties of Metals* (Pergamon, New York, 1978).
[24] H. Krakauer, A. J. Freeman, and E. Wimmer, Phys. Rev. B **28**, 610 (1983).
[25] E. Wimmer, A. J. Freeman, and H. Krakauer, Phys. Rev. B **30**, 3113 (1984).
[26] W. Eberhardt and E. W. Plummer, Phys. Rev. B **21**, 3245 (1980).
[27] H. Martensson and P. O. Nilsson, Phys. Rev. B **30**, 3047 (1984).
[28] E. W. Plummer and W. Eberhardt, Phys. Rev. B **20**, 1444 (1979).
[29] N. V. Smith, R. Lässer, and S. Chiang, Phys. Rev. B **25**, 793 (1982).

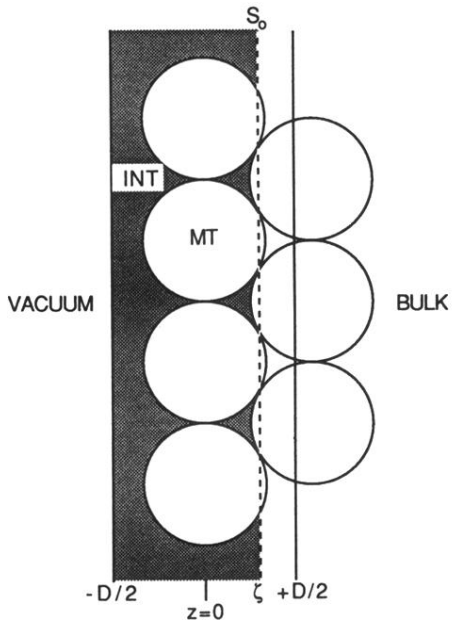

FIG. 2. The interstitial, muffin-tin, vacuum, and bulk regions. When taken to be halfway between atomic planes, the embedding interface S_0 slices through surface and bulk muffin tins.